UNIVERSITÉ LIBRE DE BRUXELLES

FACULTÉ DES SCIENCES

Mémoire présenté en vue de l'obtention du diplôme de Master en Sciences Physiques - Département de physique - Service de physique théorique

FIMPS FROM FREEZE-IN DURING A NON-STANDARD EARLY COSMOLOGY

Deraed Dylan

Supervisé par Prof. LOPEZ HONOREZ Laura

Année académique 2024-2025

Acknowledgement

I would like to express my deepest gratitude to my supervisor, Laura Lopez Honorez, whose knowledge, guidance, and support throughout this year have made this thesis possible. Her expertise and encouragement have been invaluable.
I also extend my thanks to everyone in the *Département de Physique Théorique* for the many stimulating discussions that enriched my experience. A special thank you to Lucille, Mathias, and Antoine, we faced the same challenges together, and your companionship made the journey more meaningful.
I want to thank the *Expérimentarium de Physique*, where I had the pleasure of working over the years and sharing the wonders of physics. I am especially grateful to Manu, whose passion and dedication to science communication inspired me deeply.
To my friends, thank you for your constant support. In particular, I want to thank Juliette, whose amazing talent for making any work look polished and beautiful inspired me. Without her, this thesis would not look the way it does.
Finalement, merci à ma famille pour leur soutien. Un merci tout particulier à ma filleule et à ma nièce, Romy et Solyne, leur curiosité sans fin est une source d'inspiration.

Abstract

This master thesis investigates feebly interacting massive particles (FIMPs) produced from freeze-in through the decay of a heavy particle during non-standard early cosmology. Here we focus on FIMPs momentum distribution functions and corresponding Lyman-α constraints. While previous works have primarily studied FIMP production in a radiation-dominated universe, we develop an analytical framework that extends to more general cosmological scenarios, including early matter-dominated eras and "k-dominated" eras, characterized by power-law inflaton potentials $V(\phi) \propto \phi^k$, where ϕ is the inflaton. We derive exact analytical expressions for the momentum distribution functions of FIMPs in these scenarios, distinguishing between bosonic and fermionic reheating mechanisms, which exhibit different behaviors for $k > 2$. Our analysis reveals that the scaling of the momentum distribution function at low momenta, q, changes from $q^{-1/2}$ in radiation domination to $q^{k-3/2}$ and $q^{\frac{3k-5}{2k-2}}$ for bosonic and fermionic reheating, respectively. We compute the corresponding second moments, finding significant differences that impact small-scale structure formation. By reinterpreting existing Lyman-α forest constraints from warm dark matter to FIMPs, we derive bounds on FIMP mass that show complex dependence on cosmological scenarios. These constraints indicate that, for a fixed reheating temperature, increasing the value of k weakens the bounds in the bosonic reheating scenario, while it strengthens them in the fermionic case. Our results demonstrate that the history of the early universe leaves distinctive imprints on FIMP dark matter observational signatures.

Keywords: dark matter, feebly interacting massive particles, non-standard cosmology, Lyman-α forest, early universe, freeze-in, reheating

Résumé

Ce mémoire étudie les particules massives à interaction faible (FIMPs) produites durant des scénarios cosmologiques primordiaux non-standards, en se concentrant sur leurs fonctions de distribution d'impulsion et les contraintes Lyman-α correspondantes. Alors que les travaux précédents ont principalement étudié la production des FIMPs dans un univers dominé par la radiation, nous développons un cadre analytique complet qui s'étend à des histoires cosmologiques plus générales, incluant une ère primordiale dominée par la matière et les ères "k-dominées", caractérisées par des potentiels d'inflaton en loi de puissance $V(\phi) \propto \phi^k$, où ϕ designe l'inflaton. Nous dérivons des expressions analytiques exactes pour les fonctions de distribution d'impulsion des FIMPs dans ces scénarios, distinguant les mécanismes de réchauffement bosonique et fermionique qui présentent des comportements différents pour $k > 2$. Notre analyse montre que le terme dominant les faibles impulsions varie de $q^{-1/2}$ durant l'époque dominée par la radiation à $q^{k-3/2}$ et $q^{\frac{3k-5}{2k-2}}$ pour les réchauffements bosonique et fermionique, respectivement. Nous calculons les seconds moments correspondants, trouvant des différences significatives qui impactent la formation des structures à petite échelle. En traduisant les contraintes existantes, obtenues à partir des données d'observation de la forêt Lyman-α, de la matière noire tiède aux FIMPs, nous dérivons des limites sur la masse des FIMPs qui montrent une dépendance complexe en les scénarios cosmologiques. Ces contraintes indiquent que, pour une température de réchauffement fixée, une augmentation de la valeur de k diminue les bornes inférieures dans le scénario de réchauffement bosonique, tandis qu'elle les renforce dans le cas fermionique. Nos résultats démontrent que l'histoire de l'univers primordial laisse des empreintes distinctives sur les signatures observationnelles de la matière noire FIMP.

Mots-clés : matière noire, particules massives à interaction très faible, cosmologie non-standard, forêt Lyman-α, univers primordial, gel "freeze-in", réchauffement

Contents

Acronyms

FIMP Feebly Interacting Massive Particle

DM Dark Matter

HI Neutral Hydrogen

CMB Cosmic Microwave Background

MOND Modified Newtonian Dynamics

MACHO Massive Astrophysical Compact Halo Objects

BBN Big Bang Nucleosynthesis

SM Standard Model

BSM Beyond the Standard Model

FI Freeze-In

IR Infrared

UV Ultraviolet

AGN Active Galactic Nuclei

WDM Warm Dark Matter

NCDM Non-Cold Dark Matter

LHC Large Hadron Collider

LLP Long-Lived Particle

HSCP Heavy Stable Charged Particle

DT Disappearing Track

KT Kinked Track

DL Displaced Lepton

FLRW Friedmann-Lemaître-Robertson-Walker

CDM Cold Dark Matter

RD Radiation-Dominated

MD Matter-Dominated

kD k-Dominated

EMD Early Matter-Dominated

dof degrees of freedom

BE Bose-Einstein

FD Fermi-Dirac

GUT Grand Unified Theory

WIMP Weakly Interacting Massive Particles

Introduction

Significant progress has been made in understanding the universe over the past century. A wide range of observational evidence across multiple scales, from galaxy rotation curves to the cosmic microwave background, points toward the existence of dark matter (DM). These observations indicate that dark matter accounts for approximately 25% of the total energy content of the universe. However, its nature remains one of the greatest mysteries in modern physics.

In this master thesis, we investigate feebly interacting massive particles (FIMPs), a compelling dark matter candidate. Due to their extremely weak interactions with standard model particles, FIMPs never achieve thermal equilibrium with the primordial bath. Here we focus on production through the freeze-in mechanism, a slow, out-of-equilibrium process.

The objective of this work is to understand how the early history of the universe influences FIMP production and observational signatures. While the standard cosmological model assumes that the universe was radiation-dominated at early times, alternative scenarios, in which other energy components dominate the early universe, can lead to qualitatively different outcomes for DM production. Here, in particular, we focus on the reheating period following inflation. During this period, the inflaton field oscillates around the minimum of its potential and decays into radiation. If FIMPs are produced while the universe is dominated by other components than radiation, their resulting momentum distributions and relic abundances can differ significantly.

We begin in Chapter 1 by introducing the fundamental concepts required throughout this thesis. In Chapter 2, we develop the tools necessary to compute the FIMP momentum distribution function. Starting from the Boltzmann equations, we derive analytical expressions for the distribution in various early-universe scenarios: the standard radiation-dominated era, an early matter-dominated era with a quadratic inflaton potential, and a more general "k-dominated" era characterized by a monomial inflaton potential parameterized by k. Within each scenario, we distinguish between bosonic and fermionic reheating mechanisms, which exhibit qualitatively different behavior when $k > 2$.

After establishing the momentum distributions, we compute the corresponding comoving number densities in Chapter 3, investigating how non-standard cosmologies impact the final FIMP abundance. In particular, we examine the role of the dilution factor, which arises in these scenarios. We also use the comoving number density to define the moment of the freeze-in.

Finally, in Chapter 4, we derive constraints on FIMP properties from observations of the Lyman-α forest, which probe the small-scale structure in the universe. Since non-cold dark matter candidates like FIMPs can suppress structure formation below a characteristic scale, Lyman-α observations offer powerful constraints. We reinterpret existing bounds on warm dark matter into constraints for FIMPs produced during various early cosmological epochs, highlighting how the production history shapes the viable parameter space.

My contributions

This master thesis makes several contributions to the study of FIMP dark matter in non-standard cosmologies. While the FIMP momentum distribution in a radiation-dominated universe is well known, we provide new analytical solutions for their distribution during an early matter-dominated era, including exact expressions for the second moment in Sec 2.3. We extend this analysis to general k-dominated scenarios, deriving analytical momentum distributions for both bosonic and fermionic reheating mechanisms in Secs 2.4.2 and 2.4.3 respectively. Building on these results, in Secs 4.3 and 4.4, we establish Lyman-α constraints for FIMPs produced in these eras, revealing how reheating dynamics can substantially influence dark matter phenomenology.

Chapter 1

Dark matter and cosmology

1.1 Dark Matter

The dark matter problem can be understood as a tension, a discrepancy between theoretical predictions and observational data. Such tensions are often the driving force behind scientific progress. What makes this problem particularly compelling is that multiple independent observations, at various scales, point towards the same underlying issue. In this chapter, we will examine some of these observations, identify the nature of the tension, and explore how the assumption of dark matter can resolve it. We will also introduce a candidate for particle dark matter, a feebly interacting massive particle (FIMP), and discuss the various constraints on FIMP. We will focus in particular on astrophysical constraints, such as those from the Lyman-α forest, as well as constraints from collider experiments.

1.1.1 Observations

The dark matter problem arises from a series of observations, across different scales, that are incompatible with the predictions of our current theories. In this section, we will review some of these observations.

At the galactic scale, we can study the rotational velocity of objects within a galaxy, known as the rotation curve. According to Newton's second law, the rotational velocity ($v_{\rm rot}$) as a function of the distance from the center is related to the gravitational forces. For a test mass m, such as a star, located at a distance r from the center, Newton's second law gives

$$m\frac{v_{\rm rot}^2}{r} = G\frac{mM(r)}{r^2}, \tag{1.1}$$

with $M(r)$ the mass contained within a sphere of radius r and G Newton's constant. This leads to the radial dependence for the rotational velocity

$$v_{\rm rot} = \sqrt{G\frac{M(r)}{r}}. \tag{1.2}$$

In a galaxy where most of the mass is concentrated toward the center, as would be expected from the distribution of visible matter, $M(r)$ tends to a constant at large r, implying $v_{\rm rot} \propto r^{-1/2}$. This predicts that the rotation curve should decrease with distance from the center.

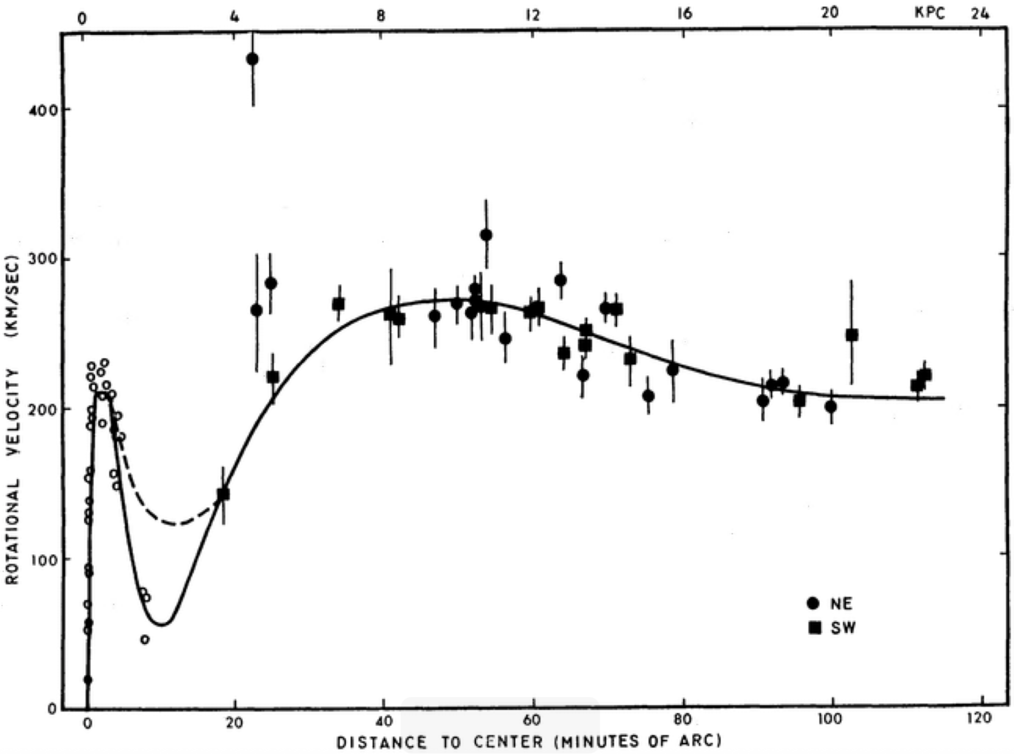

Figure 1.1: The rotation curve of the Andromeda galaxy (M31) from the 1970 paper of Vera Rubin and Kent Ford [3]. The observed flat rotation curve at large radii contradicts the expected decline, providing evidence for dark matter.

However, this contradicts the observations. They began in the late 1930s, with the PhD thesis of Horace Babcock in 1939, in which he observed the rotational velocity of the Andromeda galaxy (M31) and found that it remained high even at large distances from the center [1]. After World War II, radio astronomy experienced a significant boost due to the use of military radar equipment for astronomical observations. In 1951, Harold Ewen and Edward Purcell detected the 21 cm line, a signal emitted by neutral hydrogen (HI) atoms, which allows us to map HI clouds throughout the universe [2]. In 1970, Vera Rubin and Kent Ford used the redshift, a change in frequency due to the motion of the HI clouds, of the 21 cm line to measure the rotational velocity of M31 out to 22 kpc from the galactic center [3]. They found that, at large radii, the rotation curve remained flat, see Fig 1.1. Their measurements were more precise than previous ones and extended farther in radius. These results contradict the prediction of Newton's second law. After the results of Rubin and Ford, several papers were published investigating the rotation curves of other galaxies. Notably, in 1978, Albert Bosma published the rotation curves of 25 galaxies [4]. His work helped convince physicists that most galaxies exhibit flat rotation curves at large radii [5]. In the same year as Rubin and Ford's publication, Ken Freeman proposed the idea that missing mass in the outer regions of galaxies could explain the flat rotation curves. This missing mass can be interpreted as a halo of dark matter with a density profile $\rho(r) \propto r^{-2}$. With this assumption, $M(r) \propto r$ which cancels the radial dependence of v_{rot} resulting in a flat rotation curve at large radii [6].

At larger scales, we consider clusters of galaxies. In 1933, Fritz Zwicky studied the redshift of galaxies in the Coma cluster and used it to determine the velocity dispersion (σ_o), which quantifies the spread in velocities of galaxies within the cluster [5, 6]

$$\sigma_o = 1020\text{km/s}. \tag{1.3}$$

He applied the virial theorem, assuming the Coma cluster to be stationary, to calculate the theoretical velocity dispersion (σ_c), and compare it with the observed value. The virial theorem relates the average kinetic energy (E_k) to the potential energy (E_p)

$$\langle E_k \rangle = -\frac{1}{2} \langle E_p \rangle . \tag{1.4}$$

The average kinetic energy is given by $\langle E_k \rangle = \frac{1}{2} M\sigma^2$, with M the mass of the cluster. The average potential energy comes from gravitation, $\langle E_p \rangle = -G\frac{M^2}{r}$. From this, the velocity dispersion is

$$\sigma_c = \sqrt{2G\frac{M}{r}}. \tag{1.5}$$

Assuming the Coma cluster contains approximately 800 galaxies, each with a mass around 10^9 solar masses, Zwicky computed a theoretical velocity dispersion of $\sigma_c = 80$ km/s. To account for the large discrepancy between the observed and calculated values, Zwicky argued that the Coma cluster must be about 400 times more massive than what is inferred from visible matter. He proposed that this missing mass comes from dark matter, and famously stated that "dark matter exists in a greater density than luminous matter" [7, 8]. It is also noteworthy that in 1937, Zwicky published another paper on the Coma cluster, this time using the virial theorem and the observed velocity dispersion to estimate the cluster's total mass. He then compared this mass to the average total luminosity and found a very high mass-to-light ratio of about 500. This again led him to conclude that a significant amount of dark matter must be present in galaxy clusters. Interestingly, in that same paper, Zwicky also suggested that gravitational lensing could be used to measure the mass of galaxy clusters, a remarkably forward-looking idea [9].

Nearly seventy years later, this concept became a key tool in one of the most direct pieces of evidence for dark matter: the observation of the Bullet Cluster. This observation was made in 2006 by Douglas Clowe *et al.* [10]. They studied a system of two galaxy clusters that had collided. By analyzing the X-ray and visible light emissions, they mapped the distribution of most of the baryonic matter. They also used weak gravitational lensing, which refers to the distortion of the background due to the bending of light as it passes through the Bullet Cluster, to determine the overall distribution of mass in the system. What they found was that the bulk of the mass was located outward from the baryonic matter, in regions that do not align with the hot gas observed in X-rays. This discrepancy can be explained by the presence of dark matter in both clusters. Initially, each cluster consisted of both baryonic matter and dark matter merged together. During the collision, the baryonic matter interacted and slowed down, creating the observed X-ray and visible light signals concentrated between the clusters. In contrast, dark matter, which has suppressed interactions with standard model particles and itself, passed through the collision largely unaffected. This led to a spatial separation between the dark matter and the baryonic matter [6, 11]. In Fig. 1.2, we show the distribution of baryonic matter (from X-ray and visible light observations) and the total mass distribution (from weak lensing). The separation between the two clearly illustrates the presence of dark matter.

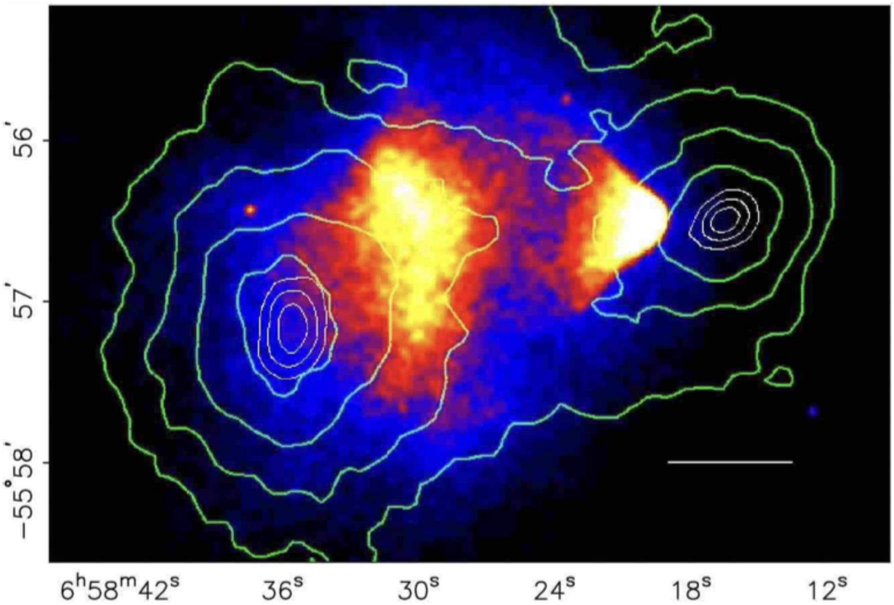

Figure 1.2: Image of the Bullet Cluster from Clowe *et al.* [10]. The distribution of baryonic matter from X-rays (blue) and visible light (red) is spatially separated from the total mass distribution determined from weak gravitational lensing (green contours), providing direct evidence for the existence of dark matter.

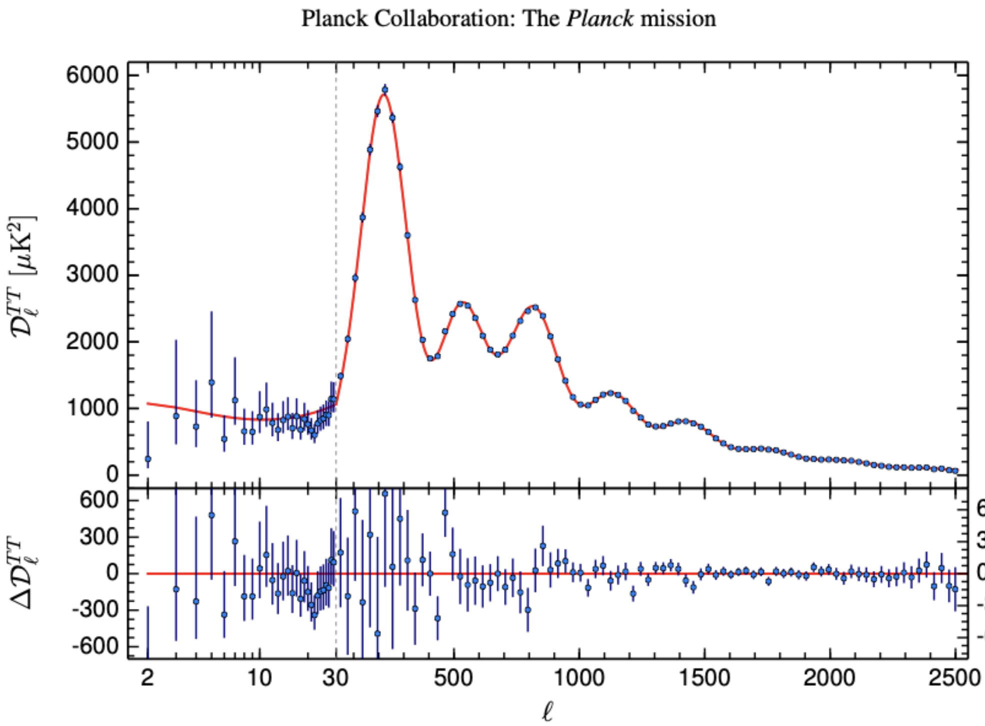

Figure 1.3: The CMB temperature power spectrum from Planck 2015 [12]. The observed positions and relative heights of the acoustic peaks, particularly the third peak compared to the second, strongly constrain the dark matter density.

The largest scale at which we have observational access is the observable universe. In the 1940s, George Gamow, Ralph Alpher, and Robert Herman, working within the framework of Big Bang theory, predicted that the cooling of the universe following the Big Bang would leave behind a relic radiation [13]. In 1964, Arno Penzias and Robert Wilson, working at Bell Labs in New Jersey, accidentally discovered an isotropic microwave signal with a temperature of approximately 3.5 Kelvin. At the same time, Robert Dicke and Jim Peebles at Princeton University were designing an experiment to detect this relic radiation. Upon learning of Penzias and Wilson's discovery, they correctly interpreted the signal as the cosmic microwave background (CMB). This led to two important papers published in 1965: one by Penzias and Wilson reporting the detection [14], and another by Dicke, Peebles, Roll, and Wilkinson interpreting it as the CMB [15].

The CMB remains one of the most precise probes of the early universe and provides strong evidence for the existence of dark matter. Its spectrum is remarkably homogeneous and follows a nearly perfect blackbody distribution at a temperature of 2.725 K. However, small anisotropies exist at the level of $\mathcal{O}(10^{-5})$, corresponding to small temperature fluctuations. These anisotropies are crucial for measuring key cosmological parameters, including the dark matter density. The CMB was released shortly after the epoch of recombination, when free electrons and protons combined to form neutral hydrogen atoms. At this point, photons decoupled from matter and began to travel freely through the universe, rendering it transparent and leaving behind the CMB as a relic. Prior to recombination, electrons, baryons, and photons were tightly coupled and behaved as a single fluid. Due to primordial quantum fluctuations, this fluid exhibited small perturbations in density and temperature. Two competing physical effects acted on these perturbations: gravitational attraction, which tends to enhance matter clustering, and photon pressure, which resists collapse. These opposing forces gave rise to acoustic oscillations, waves that propagated through the plasma at the speed of sound. These oscillations were frozen in place at recombination when the photons decoupled. Observing the imprints of these frozen waves in the CMB therefore provides a window into the physical conditions of the pre-recombination universe. To extract this information, we analyze the CMB power spectrum, which is obtained by computing the variance of the Fourier transform of the CMB temperature field. The result, shown in Fig. 1.3, displays a series of peaks, each corresponding to a mode of oscillation. The odd-numbered peaks correspond to compressions in the plasma, caused by gravitational attraction, while the even-numbered peaks represent expansion, due to photons pressure. The position and amplitude of these peaks depend on the total energy content of the universe. Dark matter plays a crucial role in shaping the CMB power spectrum. Since it interacts only gravitationally, it does not couple to the photon-baryon fluid, but it contributes to the gravitational potential wells that enhance the compression phases. As a result, dark matter tends to amplify the odd-numbered peaks. Another key feature is the Silk damping effect, which causes the amplitude of the peaks to decrease at small scales due to photon diffusion out of overdense regions. In the absence of dark matter, the second acoustic peak would be significantly higher than the third peak because of Silk damping. However, observations show that the second and third peaks have comparable amplitudes. This implies that the third peak has been enhanced, evidence of the gravitational influence of dark matter. If one could remove the Silk damping effect, the third peak would actually exceed the second. Thus, the relative heights of the second and third peaks serve as a strong signature of dark matter [16].

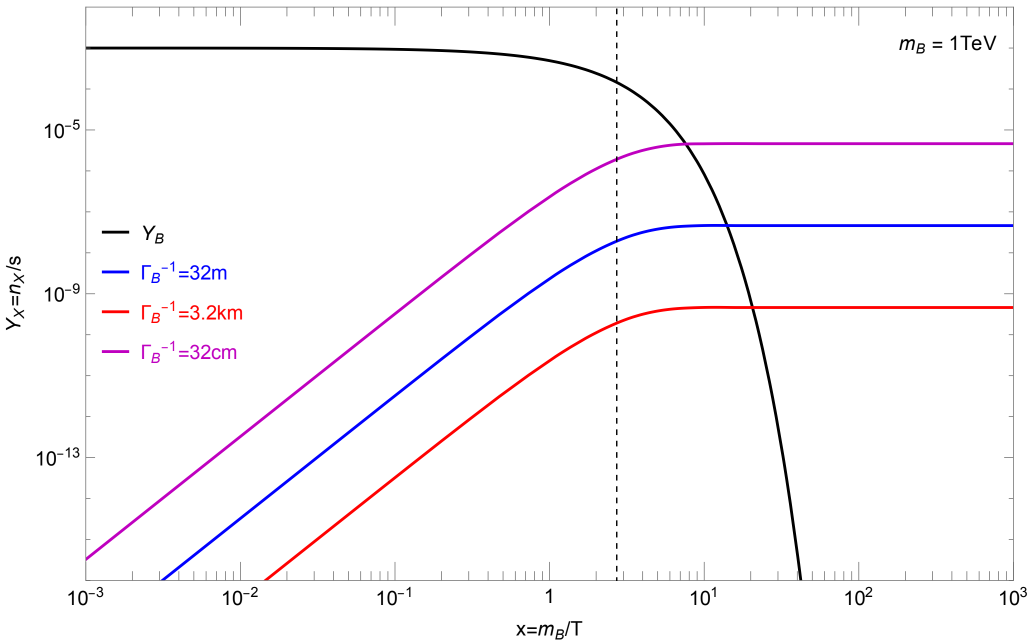

Figure 1.4: Log-log plot of the evolution of the comoving number density for FIMPs, Y_χ, as a function of the time variable $x = m_B/T$, with $m_B = 1$ TeV. The three colored curves represent Y_χ for different interaction strengths, while the black curve corresponds to the comoving number density of the mother particle B, Y_B. The dashed vertical line marks $x = 3$, the time at which the freeze-in process occurs, where the production of FIMPs is suppressed.

1.1.2 FIMP and freeze-in

All of these observations point toward the existence of dark matter. However, the true nature of dark matter remains unknown. Different approaches have been considered to account for the dark matter phenomenon. One such alternative does not invoke additional mass but instead modifies the laws of gravity. This framework, known as modified Newtonian dynamics (MOND), was introduced by Milgrom in 1982 [17]. MOND proposes a modified version of Newton's dynamics. However, this approach faces challenges to explain certain observations such as the Bullet Cluster or the CMB [17].
Another possibility is that dark matter consists of massive astrophysical compact halo objects (MACHO), such as primordial black holes, black holes that have been formed before the big bang nucleosynthesis (BBN) [5]. Alternatively, dark matter may be composed of a new particle beyond the Standard Model (BSM). In this thesis, we focus on the latter scenario.

Many particle dark matter candidates exist, but in this work, we focus on feebly interacting massive particles (FIMPs), a candidate that was formalized by J.Hall *et al.* in 2009 [18]. FIMPs interact so weakly with the standard model (SM) bath, with coupling κ in the range of $10^{-12} - 10^{-8}$, that they never reach thermal equilibrium with it [18–20]. One possible production mechanism for FIMPs is known as freeze-in (FI), a slow, out-of-equilibrium process that is infrared (IR) dominated. In this scenario, FIMPs are produced through the decay or scattering of a heavier particle, the mother particle B, which is assumed to be in thermal and chemical equilibrium with the SM bath

$$B \to A_{\rm SM} + \chi, \quad B + A'_{\rm SM} \to A_{\rm SM} + \chi,$$

where χ represents the FIMP, and $A_{\rm SM}$ and $A'_{\rm SM}$ are SM particles, with $m_B \gg m_A,\ m_\chi$. In this master thesis, we will focus on the decay of B. In this case, the trilinear interaction has the form

$$\mathcal{L}_{\rm int} \supset \kappa B \chi A_{\rm SM}, \tag{1.6}$$

with κ the coupling constant. To ensure the stability of dark matter and consistency with current observations, we impose a Z_2 symmetry under which the FIMP is odd and all standard model fields are even. We assume that in the early universe, the initial abundance of FIMPs is negligible [18, 21]. As long as the mother particle remains in chemical equilibrium, the interactions above continue to produce FIMPs. During this phase, the comoving number density of FIMPs, defined as $Y = n/s$, where s is the entropy density and n the number density, increases over time. Once the temperature drops to below the mass of B, the mother particle exits chemical equilibrium and the number density becomes Boltzmann-suppressed. When $H(T_{\rm FI}) \simeq \Gamma_B$, where H is the Hubble parameter and Γ_B is the decay rate of the mother particle, the expansion rate of the universe becomes higher than the interaction rate, and the comoving number density of FIMPs stops increasing, reaching a constant value, it freezes. To study the evolution of the comoving number density precisely, we must solve the associated unintegrated Boltzmann equation, which is detailed in Sec. 3.2. For now, we note that the comoving number density of FIMPs scales with the interaction strength as [18]

$$Y_{\rm FI} \propto \kappa^2. \tag{1.7}$$

In Fig. 1.4 we plot the comoving number density of FIMP as a function of a new time variable, $x = m_B/T$. The three colored curves correspond to different decay widths, showing that an increase in Γ_B leads to a higher comoving number density. A plateau is reached, indicating that the comoving number density becomes constant. This plateau is reached when freeze-in occurs, at $x_{\rm FI} \simeq 3$, where $x_{\rm FI}$ is defined as the time at which the first maximum of the comoving number density is reached, and is indicated by the vertical dashed line. The evolution of the comoving number density of the mother particle is represented by the black curve.

We can estimate how the comoving number density depends on the properties of the FIMP and the mother particle using a simple rule-of-thumb argument. We assume that the comoving number density of FIMPs at a given temperature is approximately

$$Y_\chi \simeq R_B(T) t(T), \tag{1.8}$$

where $R_B(T)$ is the production rate and $t(T)$ the age of the universe at the temperature T. Approximating $R_B(T) \simeq \Gamma_B m_B/T$ and $t(T) \simeq 1/H(T) \simeq M_{\rm pl}/T^2$, we obtain

$$Y_\chi(T) \simeq \frac{\Gamma_B m_B M_{\rm pl}}{T^3}. \tag{1.9}$$

This approximate solution illustrates that the freeze-in process is IR dominated, since the production of FIMPs becomes more efficient at lower temperatures [18, 20, 22]. From this estimate, we can infer the scaling of the FIMP relic density

$$\Omega_\chi h^2 \propto \frac{m_\chi \Gamma_B}{m_B^2}. \tag{1.10}$$

This dependence on the mass of B and its decay width allows these properties to be tested both in the laboratory (e.g., via collider experiments) and astrophysically (e.g., through Lyman-α constraints) [18].

1.1.3 Constraints

As we have seen in Sec. 1.1.1, dark matter, and in particular FIMPs, affects the formation of structures in the universe on both large ($\geq$ 10 Mpc) and small scales ($\leq$ 1 Mpc). By studying the structures we observe today, we can infer constraints on the properties of FIMPs.
To obtain such constraints, we need to compare the small-scale structures observed with those predicted theoretically. A powerful probe of small-scale structure is neutral hydrogen, which serves as an excellent tracer due to the abundance of hydrogen in the universe. Importantly, the hydrogen must be neutral so that it can absorb light through electronic transitions. The Lyman-α transition corresponds to an electron in a hydrogen atom transitioning from the ground state to the first excited state, with a characteristic wavelength of 121.567 nm in the ultraviolet (UV) range. To observe this absorption feature, we need a source that emits high-energy UV photons, this is provided by active galactic nuclei (AGN). AGN are supermassive black holes with accretion disks composed of hot gas, accompanied by jets aligned with their rotation axes. Depending on the orientation of these jets with respect to our line of sight, we classify AGN as blazars, jets aligned with our line of sight, or quasars, jets at a small angle. As UV photons from AGN travel through the universe toward us, they can encounter clouds of neutral hydrogen. Each time this happens, some photons are scattered out of our line of sight, producing an absorption line in the observed spectrum. However, due to the expansion of the universe, the wavelength of these photons is redshifted. This means that the farther the HI cloud is from the source, the more redshifted the corresponding absorption line will appear. A series of such absorption lines forms what is known as the Lyman-α forest in the spectra of AGN. The spectrum of a quasar at a redshift $z = 3.155$ from [23] is shown in Fig. 1.5a. By analyzing the Lyman-α forest, we can map the spatial distribution of HI clouds and infer the small-scale structure of the universe. To quantify this, we consider the transmitted flux fraction in velocity space,

$$\delta_\alpha(v) = \frac{F_{\mathrm{obs}}(v) - \bar{F}(v)}{\bar{F}(v)}, \tag{1.11}$$

where $F_{\mathrm{obs}}(v)$ is the observed flux and $\bar{F}(v)$ the average flux. From this, we define the Lyman-α flux power spectrum, corresponding to the variance of the transmitted flux, as

$$P_\alpha(k) = V \left\langle |\tilde{\delta}_\alpha(k_v)|^2 \right\rangle, \tag{1.12}$$

where $\tilde{\delta}_\alpha(k_v)$ is the Fourier transform of $\delta_\alpha(v)$ and k_v the Fourier dual of the velocity [21, 22]. In Fig. 1.5b, the Lyman-α power spectrum from [23] is shown at various redshifts. Lyman-α allows us to probe the small-scale structures only at redshift $z \sim 2 - 6$. At higher redshifts, $z \gtrsim 6$, the universe had not yet undergone reionization, so the observed flux of the Lyman-α forest would be effectively zero [24]. At lower redshifts, $z \lesssim 2$ the analysis becomes more difficult because the power spectrum becomes highly nonlinear and baryonic physics plays a significant role [25].
To obtain constraints on dark matter, we compare the measured Lyman-α flux power spectrum with the theoretical prediction. Computing this prediction requires numerical simulations, and since the scales probed by Lyman-α lie in the nonlinear regime, expensive hydrodynamical simulations are needed [22, 26]. Such simulations have been performed for warm dark matter (WDM), resulting in a constraint on its mass [27]

$$m_{\mathrm{WDM}}^{\mathrm{Ly}\alpha} \geq 5.3 \text{ keV}. \tag{1.13}$$

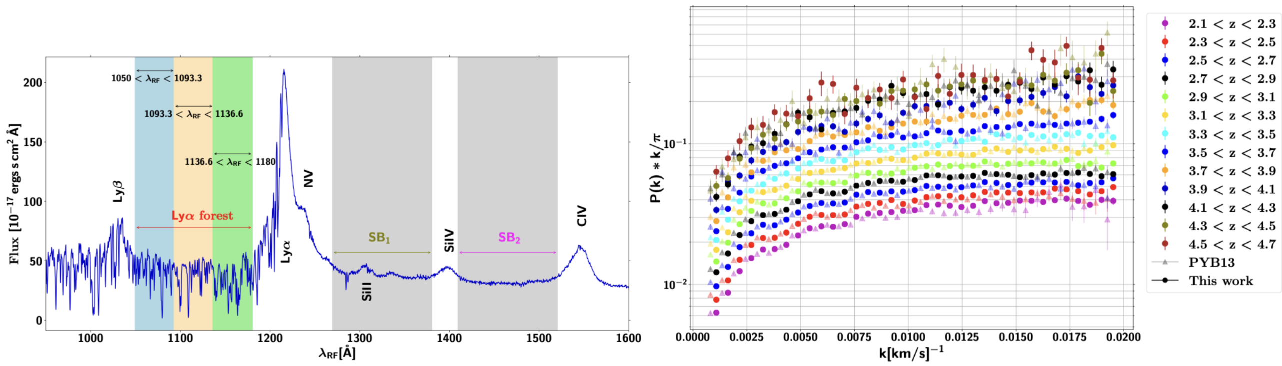

(a) (b)

Figure 1.5: **(a)** Quasar spectrum at redshift $z = 3.155$ (SDSS J114308.87+345222.2) observed by BOSS. "RF" denotes the rest frame. **(b)** Measured Lyman-α flux power spectrum at various redshifts. Both figures come from [23].

WDM belongs to a broader class known as non-cold dark matter (NCDM), characterized by non-negligible velocity dispersion at the time of structure formation. This allows NCDM particles to free-stream from overdense to underdense regions, thereby suppressing the formation of small-scale structures. Our focus, however, is on FIMPs, which also fall under the category of non-cold dark matter. Therefore, we need to interpret this Lyman-α constraint on WDM in the case of FIMPs. Several approaches exist, but the method we are interested in relies on comparing the typical velocity dispersion of FIMPs today to that of WDM [19]. The idea is to require

$$\sigma_0^{\text{FIMP}} \leq \sigma_0^{\text{WDM}}|_{\text{Ly-}\alpha}, \tag{1.14}$$

where $\sigma^X = \sqrt{\langle p^2 \rangle}/m_X$ is the root-mean-square (rms) velocity of X, with $\langle p^2 \rangle$ the second moment of the X obtained from the momentum distribution function

$$\langle p^2 \rangle = \frac{\int d^3p \; p^2 f(p)}{\int d^3p \; f(p)}. \tag{1.15}$$

This method we will develop in Chapter 4.

We can also attempt to constrain FIMPs through collider experiments. Although FIMPs interact only very weakly with the standard model, too weakly to produce detectable signals in direct dark matter searches, their relic abundance depends on the properties of a heavier mother particle B, such as its decay rate Γ_B and mass m_B, as shown in the previous section. Unlike FIMPs, the particle B can have stronger interactions with the standard model, making it potentially observable at colliders. Even though the abundance of B particles has decayed in the early universe, they can be pair-produced at collider experiments. At facilities like the large hadron collider (LHC), searches for such particles often result in displaced signals accompanied by missing energy in the final state. These signals are model-dependent. In the scenario considered here, we focus on a three-body interaction of the form

$$B \longrightarrow A_{\text{SM}} + \chi. \tag{1.16}$$

Several scenarios of this model exist, depending on the nature of the particles involved [20]. In this work, we focus on a scenario where the mother particle B is a scalar, and the FIMP χ is a

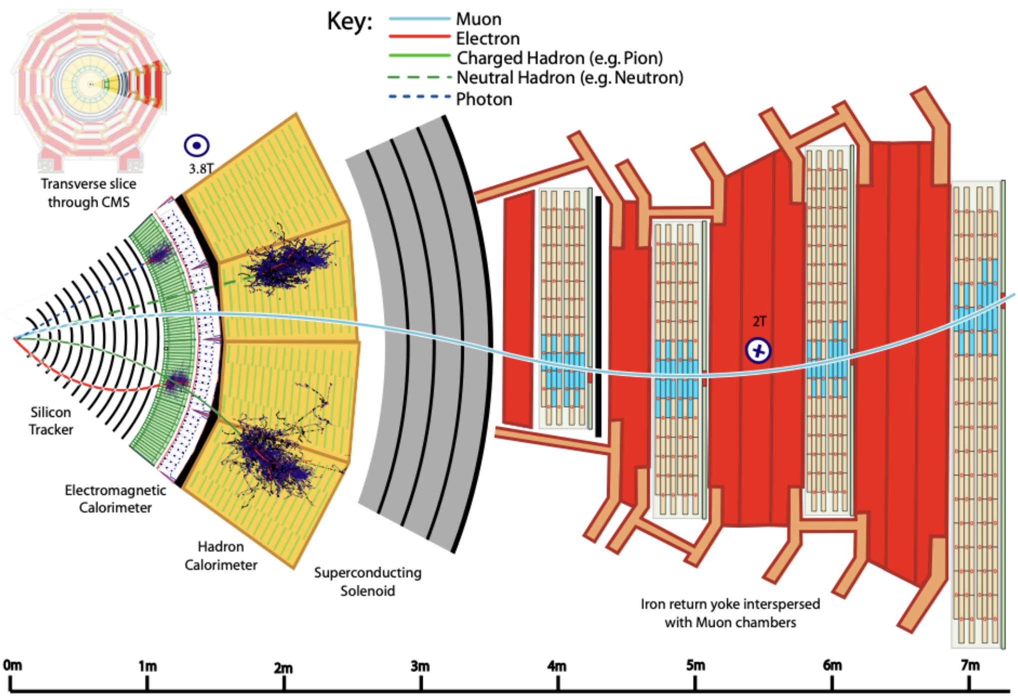

Figure 1.6: A transverse slice representation of the CMS detector taken from [28].

Majorana fermion. The relevant interaction term in the Lagrangian is given by

$$\mathcal{L}_{\text{int}} \supset \kappa \bar{\psi}_A \chi \phi_B \tag{1.17}$$

This model implies that the decay of B can have a macroscopic lifetime, since $\tau_B \propto \kappa^{-2}$. This makes B a long-lived particle (LLP), capable of travelling partially or entirely through the detector before decaying [11].

We now briefly describe the CMS and ATLAS detectors at the LHC. Both detectors are cylindrical in shape and consist of several layers. A schematic of the CMS detector is shown in Fig. 1.6. The innermost part is the tracker, where charged particles leave a charged track. A magnetic field causes their trajectories to bend, depending on their charge and momentum. Surrounding the tracker are the electromagnetic and hadronic calorimeters, which stop most particles and measure their energy. However, muons and neutrinos can pass through these layers. The outermost layer consists of muon chambers to detect the muons that penetrate the inner detectors. The architecture is designed to detect all possible observable particles. Therefore, a significant amount of missing energy could be interpreted as evidence for particles beyond the standard model, such as dark matter [11].

When searching for LLPs in CMS and ATLAS, several types of signals are investigated. One such signal comes from heavy stable charged particles (HSCPs), which appear when B is a charged particle with a decay width that satisfies $\Gamma_B^{-1} > 10$ m. In this case, B decays outside the detector but still leaves a visible track.

If the particle B is charged and has a decay length between 10 and 100 cm, it may produce signals in the tracker that vanish before exiting it. These are known as disappearing tracks (DT). If one of the decay products can be reconstructed, the result is a kinked track (KT), where the trajectory of the mother particle and its decay product form a single track with a distinctive kink at the decay point [11, 29].

Finally, if B decays into a lepton inside the tracker, the signal manifests as a lepton produced away from the primary interaction vertex. These are known as displaced leptons (DL) [11, 29]. Such type of signatures allow us to place constraints on the properties of the mother particle, such as its mass and lifetime, based on the observed relic density of FIMPs [11, 20]. In Chapter 4, we will see a projection of these constraints for a specific scenario, the leptophilic scenario, where $\psi_A = l_R$, with l_R a right-handed lepton, and ϕ_B is a scalar beyond the standard model carrying an electric charge.

1.2 Cosmology

As we saw in Sec. 1.1.1, DM influences the CMB observations, suggesting that it must have been produced in the early universe. This establishes a connection between dark matter and cosmology. The framework of cosmology will therefore be essential to derive key properties of dark matter. For this reason, this section is dedicated to introduce some of the relevant concepts.

1.2.1 Foundations of an expanding universe

In 1915, Albert Einstein published his theory of general relativity. This is a theory of gravitation that reveals a profound connection between the geometry of the universe, described by the metric ($g_{\mu\nu}$), and its contents, encoded in the energy-momentum tensor ($T_{\mu\nu}$). This relationship is captured in Einstein's field equations

$$R_{\mu\nu} - \frac{1}{2} R g_{\mu\nu} = 8\pi G T_{\mu\nu}, \tag{1.18}$$

with $R_{\mu\nu}$ the Ricci tensor and R the Ricci scalar, both derived from the metric. Just two years later, in 1917, Einstein applied his theory to describe the entire universe. The equations predicted a dynamic universe, one that could either expand or contract. Einstein did not accept this possibility and modified his equations by introducing the cosmological constant Λ, preserving a static universe [30]. In 1922, Alexander Friedmann derived solutions to Einstein's equations that described a universe in expansion [31, 32]. Subsequently, in 1927, Georges Lemaître proposed the idea that the redshift of galaxies observed in the light from distant stars could be the result of an expanding universe [33, 34]. Lemaître's hypothesis suggested that galaxies are receding from one another, a conclusion that was supported by Edwin Hubble's observations in 1929 [35]. Hubble showed, through a study of the redshift of galaxies, that there is a direct correlation between a galaxy's distance and its redshift

$$v = H_0 d, \tag{1.19}$$

with v the velocity, d the distance, and H_0 the Hubble constant today, which describes the rate of expansion of the universe at the present time. Hubble's observations confirmed the expanding nature of the universe, providing compelling evidence that the universe has a history. The field of cosmology is the study of this history.

To describe the dynamic of the universe, we need to define the correct metric to describe it and solve Einstein's field equations accordingly. It has been done by making some assumptions about the large-scale structure of our universe. The first is isotropy, meaning the universe looks the same in all directions. The second is homogeneity, meaning the universe is the same at every point in space. While these assumptions were initially adopted for mathematical simplicity, they are now supported by observations, most notably, the uniformity of the CMB (anisotropies only appear at the level of $\mathcal{O}(10^{-5})$) [36]. Together, these assumptions form the cosmological principle. A key quantity to describe an expanding universe is the scale factor, denoted $a(t)$. It characterizes how physical distances between comoving observers evolve with time. By convention, the scale factor is set to 1 today and decreases as we look back in time [37]. Another important concept, already mentioned in Sec. 1.1.1, related to the expansion, is the redshift, denoted by z. It quantifies how much the wavelength of light from distant objects has been stretched by the expansion of the universe. It is directly related to the scale factor through the relation

$$1 + z = \frac{1}{a(t)}, \tag{1.20}$$

where $a(t)$ is the scale factor at the time at which the light was emitted. A redshift of $z = 0$ corresponds to the present time, and larger values of z correspond to earlier times in the universe [37].

In 1935, Howard P. Robertson and Arthur G. Walker formalized the metric compatible with the cosmological principle. The result metric, called the Friedman-Lemaitre-Robertson-Walker (FLRW) metric, is

$$ds^2 = dt^2 - a^2(t)\left[\frac{dr^2}{1-\beta r^2} + r^2 d\Omega^2\right], \tag{1.21}$$

with $d\Omega = d\theta^2 + \sin^2 d\phi^2$ the solid angle, and β denotes the spatial curvature, which can be positive, negative, or flat. We have used the signature of the metric to be $(+ - --)$ and set $c = 1 = \hbar$ [36]. We can describe the rate at which the universe expands through the time evolution of the scale factor. It is encapsulated in the Hubble rate, defined as

$$H(t) = \frac{1}{a}\frac{da}{dt}. \tag{1.22}$$

Applying the FLRW metric to Einstein's field equations leads to a description of the evolution of the scale factor

$$H^2(t) = \frac{8\pi G}{3}\left[\rho_{\rm tot}(t) + \frac{\rho_{\rm cr} - \rho_0}{a^2(t)}\right], \tag{1.23}$$

where G is Newton's constant, $\rho_{\rm tot}(t) = \sum_i \rho_i(t)$ the total energy density of the universe (with the index i labeling the components of the universe), ρ_0 its value today. The quantity $\rho_{\rm cr} = \frac{3H_0}{8\pi G}$ is the critical density, with H_0 the Hubble rate today. The Eq. (1.23) is known as the Friedmann equation [37]. Assuming a spatially flat universe, a scenario we will adopt throughout this thesis, the Friedmann equation simplifies to

$$H^2(t) = \frac{\rho_{\rm tot}(t)}{3M_{\rm pl}^2}, \tag{1.24}$$

where $M_{\rm pl} = \sqrt{1/8\pi G} = 2.4 \times 10^{18}$ GeV is the reduced Planck mass. At large scales, the universe can be modeled as a perfect fluid. The energy-momentum tensor for such a fluid takes the form

$$T_{\mu\nu} = \begin{pmatrix} \rho(t) & 0 & 0 & 0 \\ 0 & P(t) & 0 & 0 \\ 0 & 0 & P(t) & 0 \\ 0 & 0 & 0 & P(t) \end{pmatrix}, \tag{1.25}$$

with $P(t)$ the pressure of the fluid. The energy-momentum tensor is conserved

$$D_\mu T^\mu_\nu = 0, \tag{1.26}$$

where D_μ is the covariant derivative. Imposing this for the FLRW metric leads to the continuity equation

$$\partial_t \rho(t) = -3H(t)\left(\rho(t) + P(t)\right). \tag{1.27}$$

This equation allows us to express the energy density as a function of the scale factor

$$\rho \propto a^{-3(1+w)}, \tag{1.28}$$

with $w = P/\rho$ the equation of state [37]. As examples, radiation has an equation of state $w_{\text{rad}} = 1/3$, its energy density depends on the scale factor as $\rho_{\text{rad}} \propto a^{-4}$ and the expansion rate $H \propto a^{-2}$. For matter, $w = 0$, then $\rho_{\text{mat}} \propto a^{-3}$ and $H \propto a^{-3/2}$.

1.2.2 Non-standard early cosmology

Cosmology is the study of the universe's history. Just like historians represent human history with timelines divided into distinct periods, cosmologists organize the universe's history into eras, each one defined by the type of energy that dominates the universe's energy budget at the time. This timeline begins with the big bang and continues to the present day.
Considering the FLRW universe described in the previous section, and including both a cosmological constant and cold dark matter, we obtain the standard cosmological model, known as ΛCDM. According to this model, the early universe began with the Big Bang, followed shortly by a phase of exponential expansion known as inflation. During this epoch, the energy content of the universe was dominated by a scalar field, the inflaton ϕ. Inflation ends when the inflaton starts decaying into radiation in a process known as reheating. The end of reheating initiates the radiation-dominated (RD) era. This period begins at the reheating temperature (T_R), defined by the condition $H(T_R) \sim \Gamma_\phi$, where Γ_ϕ is the inflaton decay rate. It lasts until the matter-radiation equality at $T_{\text{M-R}} \sim 1$ eV. After this, the universe enters the matter-dominated (MD) era. While the story continues, our interest lies in the earlier phases [21, 36].

In standard cosmology, the reheating temperature is assumed to be higher than the freeze-in temperature, $T_R \gg T_{\text{FI}}$. Under this assumption, the production of FIMP occurs during the standard RD era. However, there is no observational evidence that support this assumption. This motivates us to study non-standard cosmological scenarios where the reheating temperature is lower than the FI temperature, $T_R < T_{\text{FI}}$. The reheating temperature is bounded from below by Big Bang Nucleosynthesis, which requires $T_R \gtrsim 10$ MeV to ensure successful light element formation. In this scenario, FIMP are produced during the reheating period. Understanding the FIMP production in this context requires a closer look at the reheating. During this period, the inflaton oscillates around the minimum of its potential, decays into radiation, and dumps entropy. The dynamics of the universe deviate from those of the RD era. Notably, the Hubble

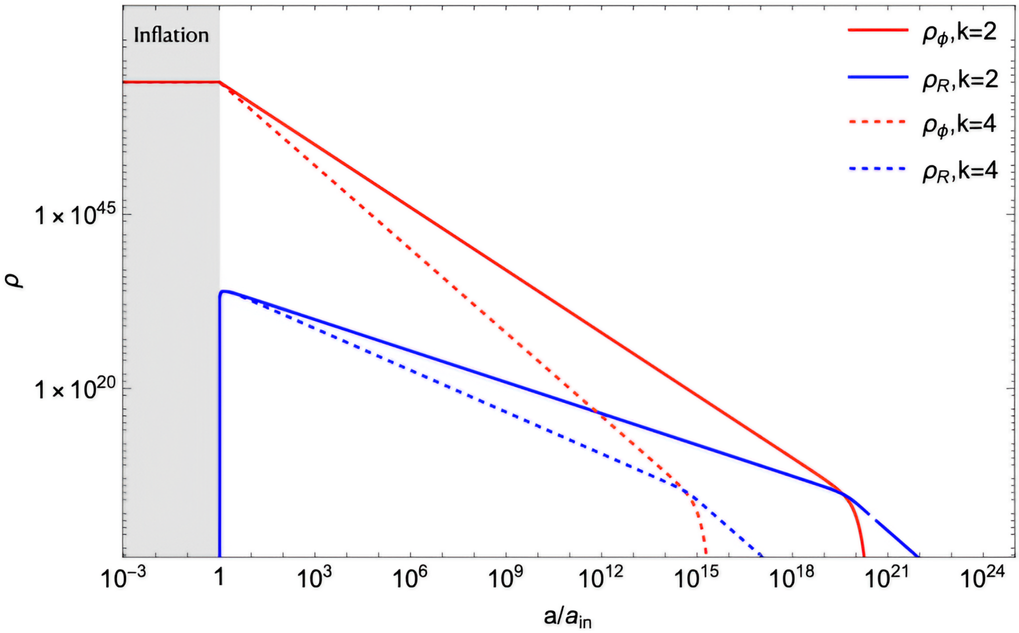

Figure 1.7: Log-log plot of the energy density (GeV^4) evolution of the inflaton (red) and radiation (blue) for $k = 2$ (solid lines) and $k = 4$ (dashed lines) as a function of the scale factor. For $k = 2$, the inflaton energy density behaves like matter, while for $k = 4$, assuming the decay rate to be constant, it exhibits a different scaling behavior, illustrating how the reheating dynamics depend on the form of the inflaton potential.

parameter and temperature scale differently with the scale factor than in RD, where $H \sim T^2$ and $T \sim a^{-1}$.
The reheating period is model dependent. We adopt a monomial potential for the inflaton field

$$V(\phi) = \lambda \frac{\phi^k}{M_{\text{pl}}^{k-4}}, \tag{1.29}$$

with $2 \leq k < 7$ and λ a dimensionless coupling [38]. This choice is consistent with the Planck 2018 observations, which have investigated various inflationary models including potentials of this form [39]. The equation of motion for the inflaton field, accounting for decay, is

$$\ddot{\phi} + (3H + \Gamma_\phi)\dot{\phi} + V'(\phi) = 0, \tag{1.30}$$

where the dot and prime denote derivatives with respect to time and ϕ, respectively. The energy density and pressure of the inflaton field are given by

$$\rho_\phi = \frac{1}{2}\dot{\phi}^2 + V(\phi) \;\text{ and }\; P_\phi = \frac{1}{2}\dot{\phi}^2 - V(\phi). \tag{1.31}$$

It allows us to define the equation of state of the inflaton as $w_\phi = P_\phi/\rho_\phi$. Due to the oscillatory behavior, w_ϕ oscillates between -1 and 1. For this reason we compute the average over some oscillations, $\langle w_\phi \rangle = \langle P_\phi \rangle / \langle \rho_\phi \rangle$ [38, 40, 41]. From Eq. (1.30), we can apply a virial theorem argument by averaging over one oscillation period, which yields

$$\left\langle \dot{\phi}^2 \right\rangle = k \left\langle V(\phi) \right\rangle . \tag{1.32}$$

leading to

$$\langle \rho_\phi \rangle = \left(\frac{k}{2} + 1 \right) \langle V(\phi) \rangle \,, \tag{1.33}$$

$$\langle P_\phi \rangle = \left(\frac{k}{2} - 1 \right) \langle V(\phi) \rangle \,, \tag{1.34}$$

and thus,

$$w_\phi = \frac{k-2}{k+2}. \tag{1.35}$$

The equation of state depends thus on the value of k [40]. A quadratic potential, with $k = 2$, yields $w_\phi = 0$, so the inflaton behaves like pressureless matter and the reheating period is identified as an early matter-dominated (EMD) era without entropy conservation. For a quartic potential, with $k = 4$, we find $w_\phi = 1/3$, corresponding to radiation-like behavior, without entropy conservation. The evolution of the inflaton energy density follows from the continuity equation, Eq. (1.27), as

$$\dot{\rho_\phi} = -\frac{6k}{k+2} H \rho_\phi - \frac{2k}{k+2} \Gamma_\phi \rho_\phi. \tag{1.36}$$

Simultaneously, the radiation energy density evolves as

$$\dot{\rho_R} = -4H\rho_R + \frac{2k}{k+2} \Gamma_\phi \rho_\phi. \tag{1.37}$$

The first term in each equation accounts for redshift due to expansion, while the second describes the inflaton's decay to radiation. The system is closed by the Friedmann equation [38]

$$H^2 = \frac{\rho_R + \rho_\phi}{3M_{\rm pl}^2}. \tag{1.38}$$

Solving for $\rho_R(a)$ allows us to define the temperature via

$$T(a) = \left(\frac{30 \rho_R(a)}{\pi^2 g_\star} \right)^{1/4} , \tag{1.39}$$

with $g_\star$ the number of relativistic degrees of freedom (dof), accounting for all particles in thermal equilibrium at a given temperature. It is defined as

$$g_\star(T) = \sum_{\text{bosons}} g_i \left(\frac{T_i}{T} \right)^4 + \frac{7}{8} \sum_{\text{fermions}} g_i \left(\frac{T_i}{T} \right)^4 , \tag{1.40}$$

with g_i the internal degrees of freedom of species i, and T_i its temperature. As the inflaton decays, it heats the thermal bath, increasing the temperature until a maximum is reached [38]. In Fig. 1.7, we show the evolution of the energy densities of the inflaton and radiation for different values of k, assuming the decay rate to be constant, highlighting how this evolution depends on the specific reheating scenario.

In this thesis, we will investigate how the production of FIMPs and the resulting Lyman-α constraints are affected in these alternative early cosmological scenarios.

1.3 Boltzmann equations

Computing this distribution is essential for understanding the properties and the evolution of dark matter. From f_χ, we can derive physically relevant quantities such as the number density

$$n_\chi = \int \frac{d^3p}{(2\pi)^3} f_\chi(x,p), \tag{1.41}$$

which can be used to obtain the comoving number, and the energy density

$$\rho_\chi = \int \frac{d^3p}{(2\pi)^3} E(p) f_\chi(x,p). \tag{1.42}$$

For particles in thermal equilibrium, the phase-space distribution $f(x^\mu, p^\mu)$, where x^μ and p^μ denote the spacetime position and four-momentum respectively, is determined by quantum statistics. Bosons follow the Bose-Einstein (BE) distribution,

$$f_{\mathrm{BE}}(E) = \frac{1}{e^{(E-\mu)/T} - 1}, \tag{1.43}$$

while fermions obey the Fermi-Dirac (FD) distribution,

$$f_{\mathrm{FD}}(E) = \frac{1}{e^{(E-\mu)/T} + 1}, \tag{1.44}$$

where E is the particle energy, and μ is the chemical potential. These distributions completely describe particles that are in kinetic and chemical equilibrium with the thermal bath. However, in Sec. 1.1.2 we mentioned that FIMPs are never in thermal equilibrium with the bath. As a result, their phase-space distribution does not follow a Bose-Einstein or Fermi-Dirac distribution. To determine the phase-space distribution of the out-of-equilibrium FIMP, we need to solve the Boltzmann equation, first introduced by Ludwig Boltzmann in 1872. Its general form reads

$$L[f_\chi] = \tilde{\mathcal{C}}[f_\chi], \tag{1.45}$$

with $L[f_\chi]$ the Liouville operator and $\tilde{\mathcal{C}}[f_\chi]$ the collision term. The left-hand side of this equation encodes the cosmology, while the right-hand side describes the particle physics.
The relativistic Liouville operator is defined as

$$L[f_\chi] = p^\alpha \frac{\partial}{\partial x^\alpha} - \Gamma^\alpha_{\beta\gamma} p^\beta p^\gamma \frac{\partial}{\partial p^\alpha}, \tag{1.46}$$

with $\Gamma^\alpha_{\beta\gamma}$ the Christoffel symbols. For a homogeneous and isotropic FLRW cosmology, the distribution depends only on time and energy, $f_\chi(x^\mu, p^\mu) = f_\chi(t, E)$. In this case, the Liouville operator becomes

$$L[f_\chi] = E\frac{df_\chi}{dt}. \tag{1.47}$$

The collision term for a generic process

$$\psi + a + b + ... \longrightarrow i + j + k + ... \, .$$

is given by

$$\tilde{\mathcal{C}}[f] = g \int \frac{d^3 p_\alpha}{(2\pi)^3} (2\pi)^4 \delta(p_\psi + p_a + ... - p_i - p_j - ...) \\ \times [|M|^2_{\psi+a+b+...\longrightarrow i+j+k+...} f_a f_b ... f_\psi (1 \pm f_i)(1 \pm f_j)... \\ - |M|^2_{i+j+k+...\longrightarrow \psi+a+b+...} f_i f_j ... (1 \pm f_a)(1 \pm f_b)...(1 \pm f_\psi)], \quad (1.48)$$

where $\alpha = a, b, ..., i, j, ...$, f_α is the distribution function of the species α, f_ψ is the distribution function of the particle of interest, and $|M|^2$ is the squared matrix element averaged over initial and summed over final states. The factor $(1 \pm f)$ accounts for the Pauli blocking, with the minus sign, or Bose-Einstein enhancing, for the plus sign. [36].
In our context, the Boltzmann equation simplifies to

$$\frac{df_\chi}{dt} = \mathcal{C}[f_\chi], \quad (1.49)$$

with $\mathcal{C}[f_\chi] = \tilde{\mathcal{C}}[f_\chi]/E$. Solving this equation gives us the full phase-space distribution of the FIMP.

Chapter 2

The momentum distribution function

We've seen, in Sec. 1.3 that knowing the phase-space distribution is crucial for understanding the properties of dark matter and for deriving observational constraints. We aim to investigate how these properties and constraints are modified when considering alternative histories of the early universe, particularly, in the case of FIMPs produced from freeze-in through the decay of a heavier mother particle B. This section is therefore dedicated to computing the momentum distribution function of FIMPs during a standard radiation-dominated era and during a reheating period for different values of k, with $2 \leq k < 7$.
In Sec. 2.1, we derive the unintegrated Boltzmann equation describing FIMP from FI produced by the decay of B for a general early cosmology. Then, we solve analytically this equation for the standard RD era, in Sec. 2.2, and the EMD era, in Sec. 2.3. Finally, Sec. 2.4, extends the analytical solution to more general reheating scenarios.

2.1 Boltzmann equation for FIMP production via three-body decay

FIMPs never achieve thermal equilibrium with the SM bath. Therefore, the momentum distribution function must be determined by solving the unintegrated Boltzmann equation, Eq. (1.49),

$$\frac{df_\chi}{dt} = \mathcal{C}[f_\chi]. \tag{2.1}$$

To proceed, we first specify this equation for the case of freeze-in production of FIMPs via the decay of a heavy mother particle B. We introduce a new time variable $x = m_B/T$ and a new momentum variable $q = p/T$. The time derivative then becomes

$$\frac{df_\chi}{dt} = \frac{\partial f_\chi}{\partial x}\frac{dx}{dt} + \frac{\partial f_\chi}{\partial q}\frac{dq}{dt}. \tag{2.2}$$

Since both the physical momentum p and the temperature T redshift as a^{-1} during expansion, their ratio $q = p/T$ remains constant, implying $dq/dt = 0$. Thus, the second term vanishes, and the left-hand side simplifies to

$$\frac{df_\chi}{dt} = -xH\xi\frac{\partial f_\chi}{\partial x}, \tag{2.3}$$

with H the Hubble rate and $\xi = \frac{d\ln T}{d\ln a}$ encodes the temperature dependence on the scale factor [19].

The relevant interaction process that we consider for DM production is the decay of B into an SM particle A and the FIMP χ

$$B \longrightarrow A + \chi. \tag{2.4}$$

The general expression for the collision term, given by Eq. (1.48), assuming negligible DM density, reduces for this decay process to,

$$\mathcal{C}[f_\chi] = \frac{1}{2g_\chi E_\chi} \int \Pi_\alpha \frac{d^3 p_\alpha}{(2\pi)^3 2E_\alpha} (2\pi)^4 \delta^4(p_A + p_\chi - p_B) f_B (1 \pm f_B)(1 \pm f_\chi)|M|^2, \tag{2.5}$$

where $\alpha = B, A$, $p = (E, \vec{p})$ denotes the four-momentum, and $|M|^2$ is the squared amplitude for the decay. We make several approximations. First, we neglect spin-statistical effects, i.e., we set $(1 \pm f) = 1$. We also assume that the mother particle B is in thermal and chemical equilibrium with the SM bath and is non-relativistic, $m_B \gg m_\chi, m_A$ [19, 21]. Its phase-space distribution function is then approximated by a Maxwell-Boltzmann distribution

$$f_B(x, q) = \frac{Y_B(x)}{Y_B^{\text{eq}}(x)} f_B^{\text{eq}}(x, q), \tag{2.6}$$

where the subscript "eq" refers to equilibrium, and for a non-relativistic particle it takes the form of a Maxwell-Boltzmann distribution with zero chemical potential. With these assumptions, the collision term simplifies to

$$\mathcal{C}[f_\chi] = \frac{1}{2g_\chi E_\chi} \int \Pi_\alpha \frac{d^3 p_\alpha}{(2\pi)^3 2E_\alpha} (2\pi)^4 \delta^4(p_A + p_\chi - p_B) f_B |M|^2. \tag{2.7}$$

We now perform the momentum integrals. By separating energy and momentum, the spatial delta function enforces momentum conservation, $\vec{p_B} = \vec{p_A} + \vec{p_\chi}$, and using the relativistic energy relation $E^2 = m^2 + \vec{p}^{\,2}$, the integral becomes

$$\mathcal{C}[f_\chi] = \frac{1}{8(2\pi)^2 g_\chi E_\chi} \int \frac{d^3 p_B}{\sqrt{m_B^2 + \vec{p_B}^2}} \frac{\delta^4(E_B - \sqrt{m_A^2 + (\vec{p_B} - \vec{p_\chi})^2} - E_\chi)}{\sqrt{m_A^2 + (\vec{p_B} - \vec{p_\chi})^2}} f_B |M|^2. \tag{2.8}$$

We now switch to spherical coordinates

$$d^3 p_B = |\vec{p_B}|^2 d|\vec{p_B}| d\cos\theta d\phi. \tag{2.9}$$

To perform the integration over the delta function, we use the identity

$$\delta(f(x)) = \frac{\delta(x - x_0)}{|f'(x_0)|}, \tag{2.10}$$

where x_0 is the root of $f(x)$ and $f'(x_0) = \frac{df}{dx}|_{x_0}$. Applying this gives the conservation of energy $E_A + E_\chi = E_B$. We obtain

$$\mathcal{C}[f_\chi] = \frac{|M|^2}{16\pi |\vec{p_\chi}| E_\chi} \int \frac{d|\vec{p_B}|}{\sqrt{m_B^2 + \vec{p_B}^2}} |\vec{p_B}| f_B. \tag{2.11}$$

Introducing the variables $\eta = E_B/T$ and $q = |\vec{p}|/T$, and assuming $T \gg m_A, m_B$, the integral simplifies to

$$\mathcal{C}[f_\chi] = \frac{|M|^2}{16\pi q E_\chi} \int d\eta f_B(\eta). \tag{2.12}$$

Assuming a Maxwell-Boltzmann distribution for f_B, using $E_\chi \simeq |\vec{p_\chi}| = qm_B/x$ and expressing the squared amplitude in terms of the decay rate as $|M|^2 = 16\pi m_B g_B \Gamma_B$, the collision term reads [19]

$$\mathcal{C}[f_\chi] = \frac{x g_B \Gamma_B}{q^2} e^{-q-\frac{x^2}{4q}}. \tag{2.13}$$

Combining the left-hand side from Eq. (2.3) with the right-hand side from Eq. (2.13), we arrive at the unintegrated Boltzmann equation for the freeze-in production of χ from the decay of B,

$$\frac{df_\chi}{dx} = -\frac{1}{\xi}\frac{g_B \Gamma_B}{q^2 H} e^{-q-\frac{x^2}{4q}} \tag{2.14}$$

A complete derivation is provided in [19]. This result holds for FIMPs produced via the decay of a non-relativistic heavy mother particle in thermal and chemical equilibrium with the SM bath. The history of the early universe, however, is encoded in the Hubble rate H and ξ, which we have not yet specified.
In the following sections, we particularize this equation to the standard RD, EMD and "k-dominated" (kD) eras, and compare the resulting distributions.

2.2 Radiation-dominated era

In this section we solve the unintegrated Boltzmann equation in the case where $T_R \gg T_{\mathrm{FI}}$, meaning dark matter is produced during a radiation-dominated era. To do this, we integrate Eq. (2.14) over $x = m_B/T$. First, we express the Hubble rate H and the factor ξ in a RD era to make their dependence on x explicit.
We start with the factor ξ, which, as a reminder, is defined as

$$\xi = \frac{d\ln T}{d\ln a}. \tag{2.15}$$

The temperature dependence on the scale factor can be derived from the evolution of the radiation energy density. In a standard RD era, the universe is dominated by radiation with an equation of state $w = 1/3$. The continuity equation, Eq. (1.28), gives the evolution of the energy density as $\rho_R \propto a^{-4}$. However, ρ_R for the radiation bath is given by

$$\rho_R = \frac{\pi^2}{30} g_\star(T) T^4. \tag{2.16}$$

It is proportional to T^4. Thus, we deduce $T \propto a^{-1}$, and therefore, assuming that $g_\star(T)$ is constant for the time of interest[1],

$$\xi = -1. \tag{2.17}$$

Next, we derive an expression for the Hubble rate H. Starting from the Friedmann equation, Eq. (1.24), and considering only the contribution of radiation, which dominates during FIMP production, we have

$$H = \frac{\sqrt{\rho_R}}{\sqrt{3} M_{\mathrm{pl}}} = \frac{T^2}{M_0}, \tag{2.18}$$

[1]The reheating temperature is constrained by Big Bang Nucleosynthesis, which occurs at temperatures around $T \sim$ MeV. At these temperatures, $g_\star(T)$ varies significantly. Therefore, assuming $g_\star(T)$ to be constant in this regime is not a reliable approximation. A more accurate treatment accounting for the temperature dependence of $g_\star(T)$ will be addressed in future work.

where

$$M_0 = M_{\rm pl}\sqrt{\frac{45}{4\pi^3 g_\star}}. \tag{2.19}$$

The second equality in Eq. (2.18) comes from the radiation energy density scaling as $\rho_R \propto T^4$. To make the dependence on x explicit, we use the relation $T = m_B/x$, yielding

$$H = \frac{m_B^2}{M_0 x^2}. \tag{2.20}$$

Substituting the expressions for ξ and H into the unintegrated Boltzmann equation, Eq. (2.14), we obtain

$$\frac{df_\chi}{dx} = \frac{g_B \Gamma_B M_0}{m_B^2 q^2} x^2 e^{-q} e^{-\frac{x^2}{4q}}. \tag{2.21}$$

This is the unintegrated Boltzmann equation describing FIMP production in a standard radiation-dominated era.

This Boltzmann equation can be solved analytically, as the integration over x in the right-hand side is a Gaussian integral. The solution gives the momentum distribution function for a radiation-dominated era

$$\boxed{f(q)|_{\rm RD} = 2\sqrt{\pi}\frac{g_B \Gamma_B M_0}{m_B^2} q^{-1/2} e^{-q}.} \tag{2.22}$$

This solution corresponds to the red dashed line in Fig. 2.1 which shows the numerical solution for the quantity $q^2 f(q)$ as a function of q. This quantity represents the contribution to the number density per unit momentum. There are two distinct behaviors depending on the momentum : at large q, the distribution is exponentially suppressed by the e^{-q} term, while at small q, the distribution is dominated by the power-law behavior $q^{-1/2}$.

We can also compute the second moment of the momentum distribution function, which, as a reminder, is given by

$$\langle p^2 \rangle = \frac{\int d^3p\, p^2 f(p)}{\int d^3p\, f(p)}. \tag{2.23}$$

In RD era, using Eq. (2.22), we obtain

$$\langle q^2 \rangle|_{\rm RD} = \frac{\Gamma\left[\frac{9}{2}\right]}{\Gamma\left[\frac{5}{2}\right]} = 8.75, \tag{2.24}$$

where $\Gamma[a]$ denotes the Gamma function, given by $\Gamma[a] = \int_0^\infty \epsilon^{a-1} e^{-\epsilon} d\epsilon$. The second moment will be useful when we will compute the Lyman-α constraint on FIMP in chapter 4.

2.3 Early matter-dominated era

Having obtained the momentum distribution in a radiation-dominated era, we proceed to study FIMP production during a reheating period ($T_R < T_{\rm FI}$), characterized by a quadratic potential, $V(\phi) \propto \phi^k$ with $k = 2$, corresponding to $w_\phi = 0$, an early matter-dominated era. Following a similar approach as in the previous section, we first derive the corresponding expressions for ξ and H, before solving the unintegrated Boltzmann equation in this regime.

To obtain both ξ and H, we need the evolution of the energy density of inflaton and radiation as a function of the scale factor. Unlike in the radiation-dominated era, the evolution is not

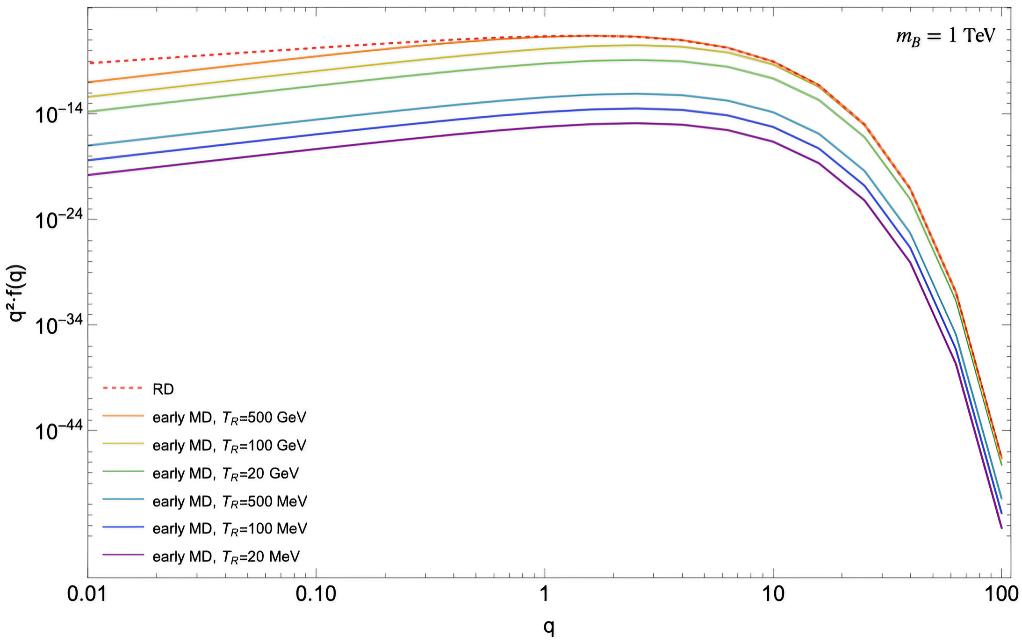

Figure 2.1: Log-log plot of the momentum distribution function of FIMP multiplied by the momentum squared, $q^2 f(q)$, as a function of the new momentum $q = p/T$ for both RD (red dashed line) and EMD (solid lines) eras, with a mother particle mass $m_B = 1$ TeV. The solid lines correspond to different reheating temperatures, ranging from $T_R = 20$ MeV (bottom) to $T_R = 500$ GeV (top).

straightforward. As explained in Sec. 1.2.2, at the end of inflation, the inflaton field oscillates around its minimum and decays into radiation. This decay affects the evolution of both the inflaton and radiation energy densities, leading to the coupled Boltzmann equations

$$\dot{\rho}_\phi = -3H\rho_\phi - \Gamma_\phi \rho_\phi, \tag{2.25}$$

$$\dot{\rho}_R = -4H\rho_R + \Gamma_\phi \rho_\phi. \tag{2.26}$$

The first term on the right-hand side of both equations represents redshift due to the expansion of the universe, as can be derived from the continuity equation, Eq. (1.27). The second term accounts for the decay of the inflaton, it decreases ρ_ϕ and increases ρ_R. In Fig. 1.7, we see the energy density of the inflaton (red) and radiation (blue) for $k = 2$ (solid lines). To close the system, we include the Friedmann equation

$$H = \frac{\sqrt{\rho_\phi + \rho_R}}{\sqrt{3} M_{\rm pl}} \tag{2.27}$$

These three equations can be solved numerically to obtain $H(a)$ and $\rho_R(a)$, and thus $T(a)$ and ξ. Integrating the Boltzmann equation over x then gives the momentum distribution function in an early matter-dominated era. The numerical solutions are shown in Fig. 2.1, which displays $q^2 f(q)$ as a function of q. The solid lines correspond to different reheating temperatures, while the dashed line corresponds to RD era, for $m_B = 1$ TeV. The orange solid line corresponds to a reheating temperature of $T_R = 500$ GeV, which exceeds the FI temperature, $T_{\rm FI} \sim 170$ GeV, computed in the next chapter. Thus, the orange line corresponds to FIMP production during a standard RD era, rather than during reheating. Accordingly, it matches the red dashed line, integrating under the curves yields equivalent relic densities, $\Omega_\chi^{\rm EMD}|_{T_R=500{\rm GeV}} \simeq 7.3\times10^{-7} \simeq \Omega_\chi^{\rm RD}$. As observed, the momentum distribution in EMD era closely resembles that in RD era. They coincide at high momentum, while at low momentum the slope differs. Changing the reheating temperature mainly shifts up and down the momentum distribution.

This similarity suggests that an analytical solution for the momentum distribution function in an EMD era might exist. In the previous section, we derived the analytical solution for the RD era, Eq. (2.22), and noted that at high momentum, the dominant term is e^{-q}. A similar behavior is expected here. At low momentum, while the RD distribution scaled as $q^{-1/2}$, we anticipate a different power-law dependence in the EMD case. To find an analytical solution, we solve the coupled Boltzmann and Friedmann equations.
First, we consider the evolution of the inflaton energy density. Before reheating, we assume that $H \gg \Gamma_\phi$, allowing us to neglect the decay term. Thus, the inflaton energy density redshifts as matter [20, 38, 42]

$$\rho_\phi = \rho_\phi(a_{\rm in}) \left(\frac{a_{\rm in}}{a}\right)^3 , \tag{2.28}$$

with $a_{\rm in} = a(T_{\rm in})$ the scale factor at the end of inflation. Substituting this expression into the Friedmann equation and neglecting the radiation energy density ρ_R during reheating, we obtain an approximate expression for the Hubble rate

$$H \simeq \frac{\sqrt{\rho_\phi}}{\sqrt{3}M_{\rm pl}} = \frac{\sqrt{\rho_\phi(a_{\rm in})}}{\sqrt{3}M_{\rm pl}} \left(\frac{a_{\rm in}}{a}\right)^3 . \tag{2.29}$$

This leads to a non-homogeneous first-order differential equation for ρ_R whose solution reads

$$\rho_R = \frac{2\sqrt{3}}{5} M_{\rm pl}\Gamma_\phi \sqrt{\rho_\phi(a_{\rm in})} \left[\left(\frac{a_{\rm in}}{a}\right)^{3/2} - \left(\frac{a_{\rm in}}{a}\right)^4\right] \tag{2.30}$$

Initially, at $a = a_{\rm in}$, $\rho_R = 0$, as expected. Relating ρ_R to the temperature via Eq. (1.39), we recover the scaling behavior during reheating. The temperature reaches a maximum, $T_{\rm max}$, at $a_{\rm max} = (8/3)^{2/5} a_{\rm in}$, after which

$$T(a) = T_{\rm max} \left(\frac{a_{\rm max}}{a}\right)^{3/8} . \tag{2.31}$$

Thus, Eq. (2.30), tell us that, during EMD, $\rho_R \propto a^{-3/2}$ and $T \propto a^{-3/8}$, which evolves more slowly than during the radiation-dominated era. The corresponding ξ factor is

$$\xi = -\frac{3}{8}. \tag{2.32}$$

We now express H explicitly as a function of x. Using Eq. (2.31), we write

$$H = \frac{\sqrt{\rho_\phi(a_{\rm in})}}{\sqrt{3}M_{\rm pl}} \left(\frac{T}{T_{\rm max}}\right)^4 \qquad [T_{\rm max} > T > T_R] . \tag{2.33}$$

Since the reheating temperature is a parameter of our theory, we want to express the Hubble rate in terms of T_R. The reheating temperature is related to $T_{\rm max}$ through the definition $H(T_R) \simeq \Gamma_\phi$, allowing us to express H as

$$H = \frac{1}{\tilde{M}_0}\frac{T^4}{T_R^2} = \frac{1}{\tilde{M}_0}\frac{m_B^4}{T_R^2 x^4} \qquad [T_{\rm max} > T > T_R] , \tag{2.34}$$

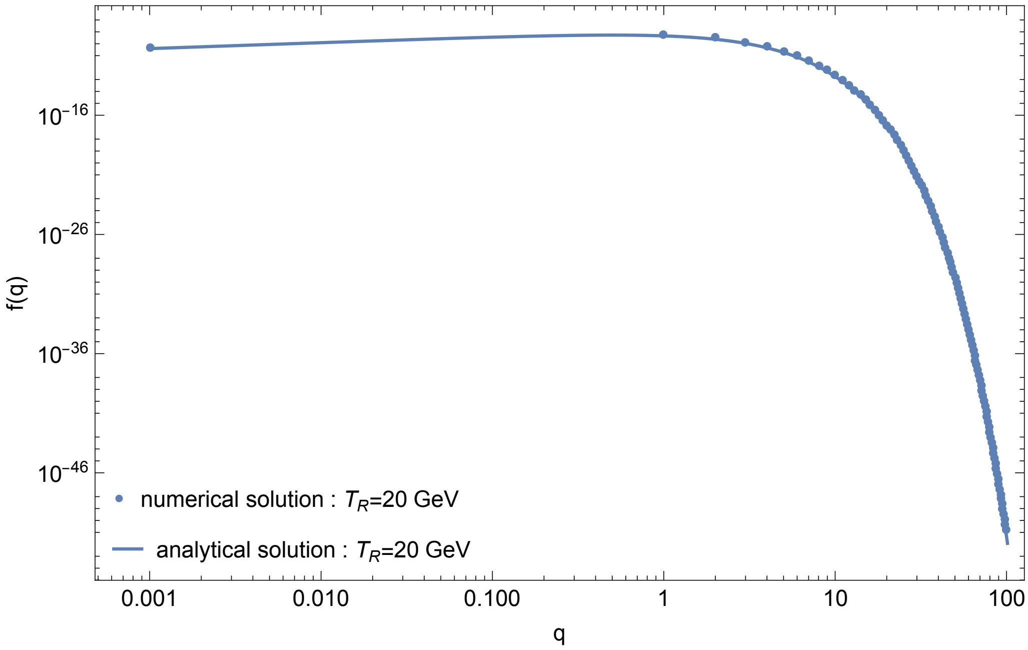

Figure 2.2: Log-log plot of the momentum distribution function of FIMP produced during an EMD era, comparing the analytical solution (solid line) with the numerical results (dots), as a function of $q = p/T$, for a reheating temperature $T_R = 20$ GeV and with a mother particle mass $m_B = 1$ TeV. The plot shows good agreement between both approaches across the full momentum range.

where

$$\tilde{M}_0 = (0.3)^4 M_{\rm pl} \sqrt{\frac{2\pi^2 g_\star}{15}}. \tag{2.35}$$

Substituting ξ and the Hubble rate H into the unintegrated Boltzmann equation, Eq. (2.14), gives

$$\frac{df_\chi}{dx} = \frac{8}{3} \frac{g_B \Gamma_B \tilde{M}_0}{m_B^2 q^2} \frac{T_R^2}{m_B^2} x^4 e^{-q} e^{-\frac{x^2}{4q}}. \tag{2.36}$$

This is a Gaussian integral in x, which can be solved analytically. The result is the momentum distribution function for an EMD era

$$\boxed{f(q)|_{\rm EMD} = 2\sqrt{\pi} \frac{g_B \Gamma_B \tilde{M}_0}{m_B^2} \left(\frac{T_R}{m_B}\right)^2 q^{1/2} e^{-q}.} \tag{2.37}$$

Comparing with the RD era solution, Eq. (2.22), we find that at high momenta, the distributions coincide, both dominated by the e^{-q} exponential. However, at low momenta, the EMD distribution scales as $q^{1/2}$ rather than $q^{-1/2}$, explaining the change in slope observed in Fig. 2.1. This difference originates from distinct scaling of the Hubble rate with x. In Fig. 2.2, we compare the analytical (solid line) and numerical (dot) solution of the momentum distribution function for FIMP produced in EMD era, for $T_R = 20$ GeV and $m_B = 1$ TeV.
We also compute the second moment of the momentum distribution for FIMP production during an EMD era

$$\langle q^2 \rangle |_{\rm EMD} = \frac{\Gamma\left[\frac{11}{2}\right]}{\Gamma\left[\frac{7}{2}\right]} = 15.75. \tag{2.38}$$

This value is higher than in the RD era, indicating that FIMPs produced during reheating are, on average, hotter, they carry more momentum relative to their mass at the time of production. Consequently, these particles have a larger free-streaming length compared to FIMPs produced during RD era, potentially leading to a stronger suppression of small-scale structure.

2.4 Generalization to k-dominated early cosmology

In the previous section, we derived an analytical solution for the momentum distribution function of FIMPs produced via FI from the decay of a heavy mother particle, during a reheating period described by a quadratic potential. In this section, we aim to generalize this solution to arbitrary monomial potentials for the inflaton,

$$V(\phi) = \lambda \frac{\phi^k}{M_{\rm pl}^{k-4}}. \tag{2.39}$$

To do so, we first introduce additional parameters that capture the relevant features of the reheating process, in Sec. 2.4.1. We then derive the momentum distribution function for fermionic reheating (FR) in Sec. 2.4.3, and for bosonic reheating (BR) in Sec. 2.4.2.

2.4.1 Fermionic and Bosonic reheating

If we want to generalize the analytical solution for the momentum distribution function to arbitrary values of k, particularly for $2 < k < 7$, we need a more detailed understanding of the inflaton decay process. Up to now, we have emphasized that choosing a value of k determines the equation of state during reheating, which sets the time evolution of the Hubble rate and thus affects the freeze-in production of FIMPs. However, for $k > 2$, the choice of k also impacts the inflaton's decay rate. The inflaton decay rate is a key ingredient controlling the evolution of both the inflaton and radiation energy densities. We have already seen that the behavior of these densities changes for different values of k, assuming Γ_ϕ constant, as illustrated in Fig. 1.7. In this section, we will explain how, for $2 < k < 7$, the decay rate Γ_ϕ becomes field-dependent, and how this dependence impacts the momentum distribution function [38, 41, 43].
During the reheating period, the inflaton begins to oscillate around its potential minimum and decays into high-energy particles. We consider two possible decay channels: bosonic reheating, where the inflaton decays into a pair of bosons, and fermionic reheating, where it decays into a pair of fermions. The interaction terms in the Lagrangian are, respectively,

$$\mathcal{L}_{\rm int} \supset \mu\phi XX \quad \text{and} \quad \mathcal{L}_{\rm int} \supset y\phi f\bar{f}, \tag{2.40}$$

where X and f denote a boson and a fermion, respectively, μ is a dimensionful coupling constant, and y is a Yukawa coupling [41]. The subtlety introduced when $k > 2$ is due to the field dependence of the inflaton mass. Recall that the dynamics of the field is governed by the equation of motion

$$\ddot{\phi} + (3H + \Gamma_\phi)\dot{\phi} + V'(\phi). \tag{2.41}$$

We parametrize the inflaton field as

$$\phi(t) = \phi_0(t) P(t), \tag{2.42}$$

where $\phi_0(t)$, the envelope, encodes the effect of redshift and decay and $P(t)$ the anharmonicity of the short timescale oscillations [41]. The decay rate of the inflaton will involve the mass of the inflaton, obtained from the potential

$$m_\phi^2(t) = V''(\phi) = k(k-1)\lambda \frac{\phi(t)^{k-2}}{M_{\text{pl}}^{k-4}}. \tag{2.43}$$

We see that when $k > 2$ the mass of the inflaton depends on the field. Therefore, the oscillations of the inflaton affect m_ϕ, and consequently Γ_ϕ. This is not the case when $k = 2$, where m_ϕ is constant. This is why we did not introduce this subtlety earlier.
To deal with this complication, we need to take an average over oscillations. We now proceed to compute the decay rates for both scenarios.

We begin with the bosonic reheating process. In this scenario, the inflaton could decay into Higgs particles, or, if we consider a Majorana dark matter scenario, into the mother particle B [38]. Assuming that the mass of the final state particles is negligible compared to the inflaton mass, the inflaton decay rate, averaged over oscillations, is given by

$$\Gamma_{\phi\to XX}(t) = \frac{\mu_{\text{eff}}^2(k)}{8\pi m_\phi(t)}, \tag{2.44}$$

where μ_{eff} is the effective coupling due to the average over oscillations. It is related to the coupling μ by

$$\mu_{\text{eff}}^2(k) = \frac{(k+2)(k-1)}{4}\frac{\omega}{m_\phi}\alpha_\mu(k,\mathcal{R})\mu^2, \tag{2.45}$$

where ω is the frequency of oscillations of ϕ, defined as

$$\omega = m_\phi \sqrt{\frac{\pi k}{2(k-1)}}\frac{\Gamma(\frac{k+2}{2k})}{\Gamma(\frac{1}{k})}. \tag{2.46}$$

The factor $\alpha_\mu(k,\mathcal{R})$ is referred to as the coupling strength, where $\mathcal{R} \propto (m_{\text{eff}}/m_\phi)^2$ is a kinematic factor involving the effective mass m_{eff} of the decay products. When $\mathcal{R} \ll 1$, the effective mass induced by the inflaton is negligible, and the decay products can be considered effectively massless. However, as k increases, $\mathcal{R}$ grows significantly. In particular, as k approaches 7, one enters a regime where $\mathcal{R} \gg 1$, and the inflaton decay transitions from a perturbative to a non-perturbative process. Such regimes require a dedicated treatment beyond the framework developed here, which assumes perturbative decay throughout. This justifies restricting our analysis to values of $k < 7$, ensuring the validity of the perturbative approach [41]. It is also worth noting that for $k = 2$, one finds $\mu_{\text{eff}} = \mu$, since the decay rate is independent of the inflaton's oscillations in this case [38, 41, 43].

For fermionic reheating, we consider the inflaton decaying into a pair of fermions. Because fermions are chiral particles, the inflaton cannot decay directly into them, we need to introduce a vectorlike or Majorana fermion as an intermediate state [38]. This state could be identified as the mother particle B. Under the same assumption that the mass of the final state fermions is negligible compared to the inflaton mass, the decay rate, averaged over oscillations, is

$$\Gamma_{\phi\to f\bar{f}}(t) = \frac{y_{\text{eff}}^2(k)}{8\pi} m_\phi(t), \tag{2.47}$$

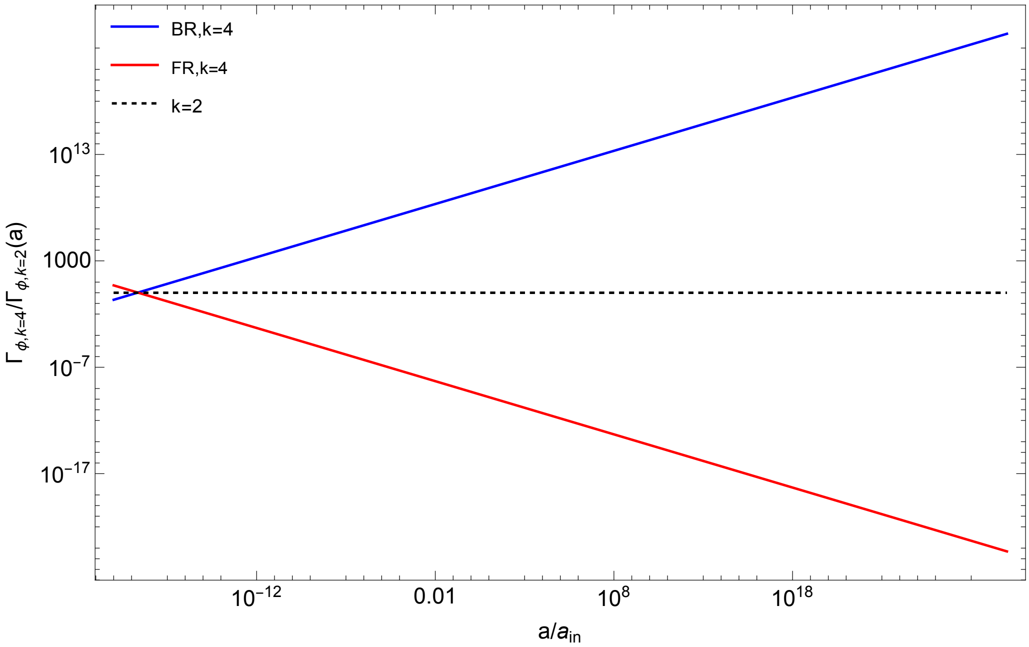

Figure 2.3: Log-log plot of the decay rate of the inflaton as a function of the scale factor for both bosonic (blue) and fermionic (red) reheating scenarios with $k = 4$, and for $k = 2$ (Black dashed). For $k = 2$, the decay rate remains constant over time, yielding identical behavior in both scenarios. In contrast, for $k = 4$, the decay rate increases with time in the bosonic case, as the inflaton field decreases, while it decreases in the fermionic case, highlighting the fundamentally distinct dynamics when $k > 2$.

where y_{eff} is the effective coupling due to the average over oscillations, related to the coupling y as

$$y^2_{\text{eff}}(k) = \frac{\omega}{m_\phi}\alpha_y(k, \mathcal{R})y^2. \tag{2.48}$$

As before, for $k = 2$, we recover $y_{\text{eff}} = y$ [38, 41].
The difference betwexen bosonic and fermionic reheating arises from the distinct dependence of the decay rate on the inflaton mass, which in turn leads to different dependence of the field. In Fig. 2.3, we observe the evolution of $\Gamma_\phi(a)$ as a function of the scale factor for both reheating scenarios. The two cases exhibit opposite behaviors: for bosonic reheating, $\Gamma_{\phi\to XX}(t) \propto 1/m_\phi(t) \propto \phi^{\frac{2-k}{2}}(t)$, which for $k = 4$ gives $\Gamma_{\phi\to XX}(t) \propto \phi^{-1}$. Consequently, as the universe expands, $\phi(t)$ decreases and the decay rate increases. In contrast, for fermionic reheating, $\Gamma_{\phi\to f\bar{f}}(t) \propto m_\phi(t) \propto \phi^{\frac{k-2}{2}}(t)$, which for $k = 4$ yields $\Gamma_{\phi\to f\bar{f}}(t) \propto \phi(t)$. As the universe expands, $\phi(t)$ decreases, and the decay rate decreases as well.
In the next two sections, we will derive how does the evolution of the energy density is affected by these results and compute the momentum distribution function for both bosonic and fermionic reheating, respectively. For both cases, the evolution of the inflaton and radiation energy densities follows from the continuity equation, Eq. (1.27), modified to include the decay term

$$\dot{\rho_\phi} = -\frac{6k}{k+2}H\rho_\phi - \frac{2k}{k+2}\Gamma_\phi(t)\rho_\phi, \tag{2.49}$$

$$\dot{\rho_R} = -4H\rho_R + \frac{2k}{k+2}\Gamma_\phi(t)\rho_\phi, \tag{2.50}$$

where $\Gamma_\phi(t)$ denotes the time-dependent decay rate of the inflaton, which differs in form between the bosonic and fermionic cases. Assuming $H \gg \Gamma_\phi(t)$, valid at early times during reheating, the decay term can be neglected in Eq. (2.49), leading to the approximate solution

$$\rho_\phi(a) = \rho_\phi(a_{\rm in}) \left(\frac{a_{\rm in}}{a}\right)^{\frac{6k}{k+2}} . \tag{2.51}$$

Neglecting radiation in the Friedmann equation during this phase, the Hubble parameter evolves as

$$H(a) \simeq \frac{\sqrt{\rho_\phi}}{\sqrt{3}M_{\rm pl}} = \frac{\sqrt{\rho_\phi(a_{\rm in})}}{\sqrt{3}M_{\rm pl}} \left(\frac{a_{\rm in}}{a}\right)^{\frac{3k}{k+2}} \qquad [T_{\rm max} > T > T_R] . \tag{2.52}$$

2.4.2 Momentum distribution function for bosonic reheating

To derive the momentum distribution function for FIMPs during a bosonic reheating, we start from the unintegrated Boltzmann equation, Eq. (2.14). We apply the same method as used for RD and EMD eras, expressing ξ and H in terms of $x = m_B/T$, and then performing the integration.

Using the solutions for the inflaton energy density and the Hubble parameter given in Eqs. (2.51) and (2.52), together with the envelope approximation $\rho_\phi(t) = V(\phi_0(t))$, which allows us to relate the mass of the inflaton to its energy density as [41]

$$m_\phi^2(t) \simeq k(k-1)\lambda^{2/k} M_{\rm pl}^{\frac{2(4-k)}{k}} \rho_\phi^{\frac{k-2}{k}}(t), \tag{2.53}$$

we solve for ρ_R, yielding

$$\rho_R = \frac{\sqrt{3}}{8\pi}\frac{1}{1+2k}\sqrt{\frac{k}{k-1}}\frac{\mu_{\rm eff}^2}{\lambda^{1/k}} M_{\rm pl}^{\frac{2k-4}{k}} \rho_\phi^{1/k}(a_{\rm in}) \left[\left(\frac{a_{\rm in}}{a}\right)^{\frac{6}{2+k}} - \left(\frac{a_{\rm in}}{a}\right)^4\right] . \tag{2.54}$$

Figure 2.4a shows the evolution of the energy densities of the inflaton (green) and radiation (blue) as a function of the scale factor, for both $k = 2$ (solid lines) and $k = 4$ (dashed lines). We observe that reheating occurs significantly earlier for $k = 4$, around $a \sim 10^{10}$, compared to $a \sim 10^{22}$ for $k = 2$. This can be understood by examining Fig. 2.3, which shows that $\Gamma_\phi(k = 4) > \Gamma_\phi(k = 2)$. A larger decay rate implies a shorter inflaton lifetime, i.e., $\tau_\phi(k = 4) < \tau_\phi(k = 2)$, and therefore, reheating takes place earlier for larger k. Thus, during bosonic reheating we find $\rho_R \propto a^{-\frac{6}{2+k}}$ and $T \propto a^{-\frac{3}{4+2k}}$, leading to the corresponding factor ξ

$$\xi = -\frac{3}{4+2k}. \tag{2.55}$$

The radiation energy density reaches a maximum at $a_{\rm max} = a_{\rm in}\left(\frac{2k+4}{3}\right)^{\frac{k+2}{4k+2}}$, where the temperature is maximum. From there, the temperature redshifts as

$$T = T_{\rm max}\left(\frac{a_{\rm in}}{a}\right)^{\frac{3}{4+2k}} . \tag{2.56}$$

Using definition of the reheating temperature, the Hubble rate can be expressed as

$$H = \frac{1}{M_0}\frac{T^{2k}}{T_{\rm R}^{2k-2}} = \frac{1}{M_0}\frac{m_B^{2k}}{T_{\rm R}^{2k-2}x^{2k}} \qquad [T_{\rm max} > T > T_R] . \tag{2.57}$$

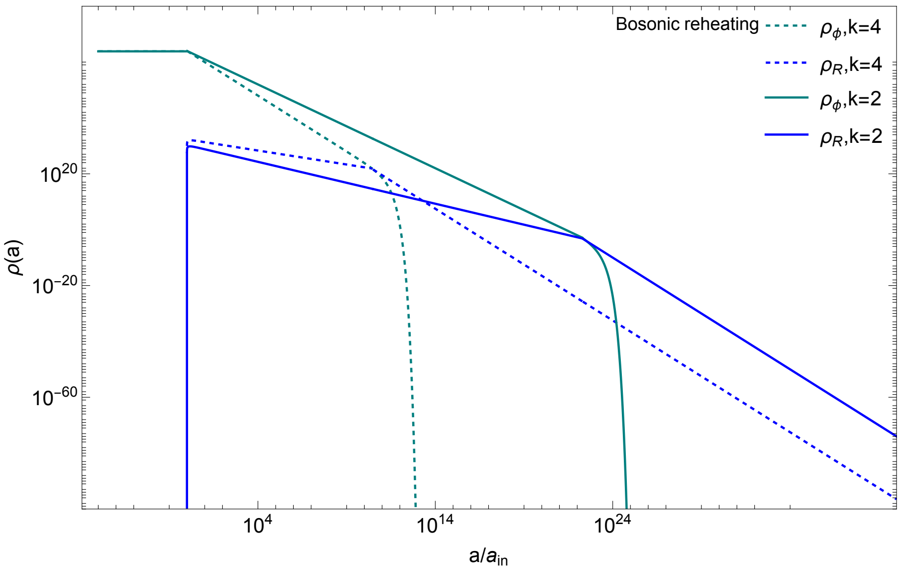

(a)

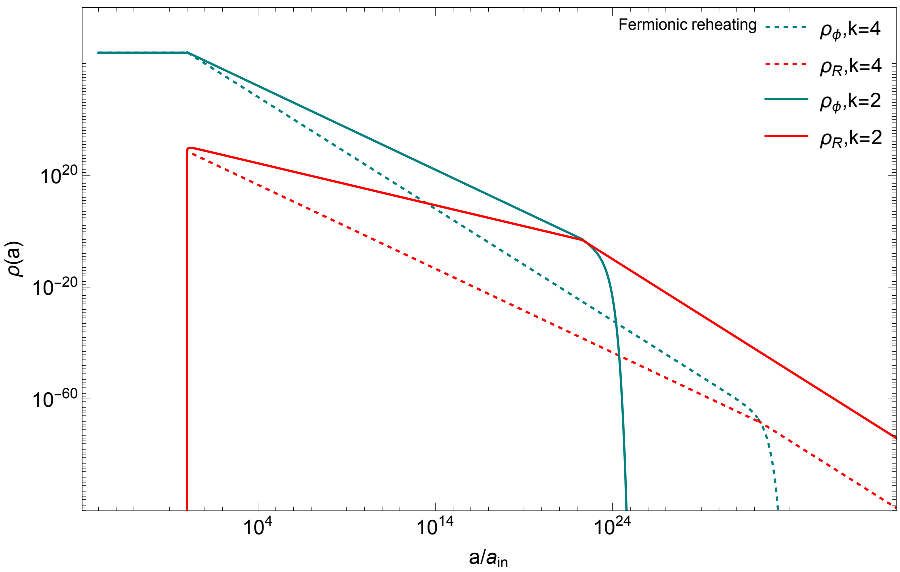

(b)

Figure 2.4: Log-log plot of the evolution of the energy densities (GeV^4) of the inflaton (green) and radiation for **(a)** bosonic reheating (blue) and **(b)** fermionic reheating (red) as a function of the scale factor for $k = 2$ (solid lines) and $k = 4$ (dashed lines). We have considered the parameter values $\mu = 10^{-13}$ Mpl, $y = 10^{-7}$, and an initial inflaton energy density $\rho_\phi(a_{\rm in}) = M_{\rm gut}^4$, where $M_{\rm gut} = 10^{16}$ is the grand unified theory (GUT) scale.

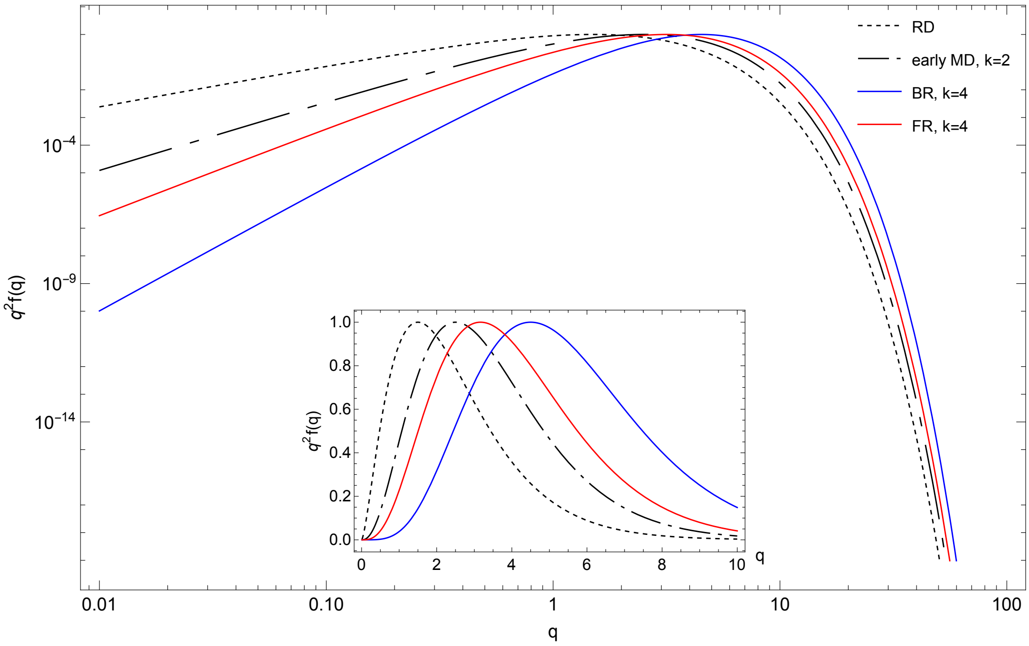

Figure 2.5: Log-log plot of the normalized momentum distribution functions, $q^2 f(q)$, as a function of the momentum $q = p/T$, for FIMPs produced under different cosmological scenarios with $m_B = 1$ TeV. The dashed line corresponds to the standard RD case, while the solid black line represents an EMD era with $k = 2$. The dot-dashed blue and red curves show the distributions for bosonic and fermionic reheating with $k = 4$, respectively. The inset is a linear plot of the same distributions, zooming in to highlight the position of the peak.

Substituting ξ and H into Eq. (2.14) gives

$$\frac{df_\chi}{dx} = \left(\frac{4+2k}{3}\right) \frac{g_B \Gamma_B M_0}{m_B^2 q^2} \left(\frac{T_R}{m_B}\right)^{2k-2} x^{2k} e^{-q} e^{-\frac{x^2}{4q}}. \tag{2.58}$$

This is a Gaussian integral in x, which can be solved analytically. The result is the momentum distribution function of FIMPs for $2 < k < 7$ during a bosonic reheating

$$\boxed{f(q)|_{\mathrm{BR}} = 2^k \sqrt{\pi}\ (2k-1)! \left(\frac{4+2k}{3}\right) \frac{g_B \Gamma_B M_0}{m_B^2} \left(\frac{T_R}{m_B}\right)^{2k-2} q^{k-3/2} e^{-q}.} \tag{2.59}$$

Figure 2.5 shows $q^2 f(q)$ as a function of q for bosonic reheating with $k = 4$ (solid blue), along with the corresponding momentum distribution functions for the standard RD era (dashed black) and an EMD era (solid black). In the bosonic reheating case with $k = 4$, the distribution scales as $f(q) \propto q^{5/2}$ at low momentum, which is steeper than the EMD case ($f(q) \propto q^{1/2}$) and the RD case ($f(q) \propto q^{-1/2}$). This steeper rise at low q is clearly visible in Fig. 2.5. At high momentum, all distributions, including those from bosonic reheating, EMD and RD, exhibit the same exponential suppression, scaling as e^{-q}.
The second moment of the momentum distribution function, defined by Eq. (2.23), is

$$\langle q^2 \rangle\,|_{\mathrm{BR}} = \frac{\Gamma[\frac{7}{2}+k]}{\Gamma[\frac{3}{2}+k]}. \tag{2.60}$$

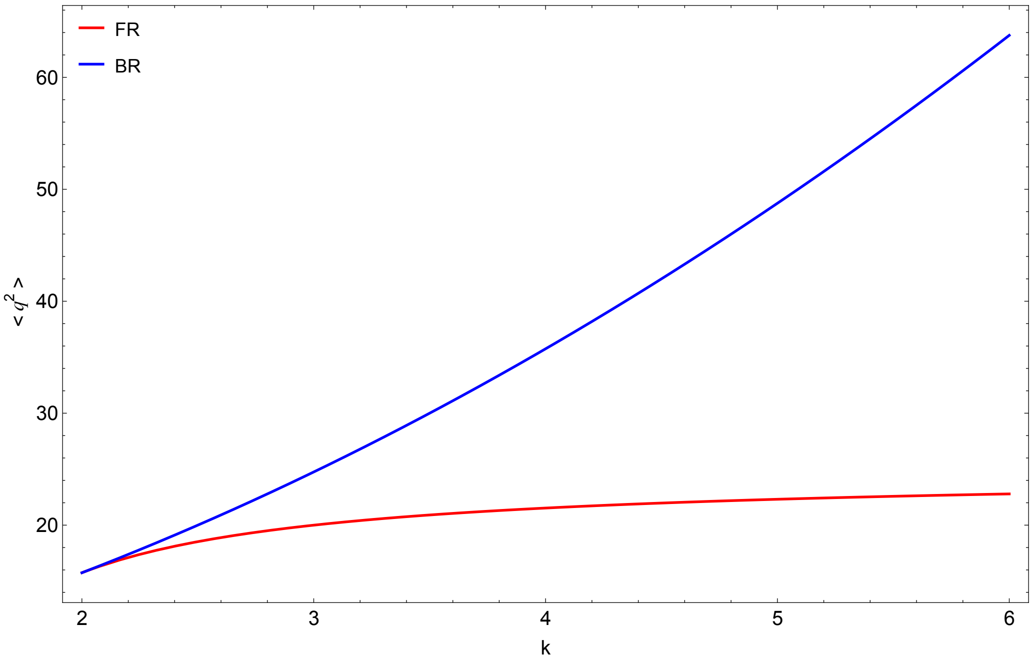

Figure 2.6: Second moment of the FIMP momentum distribution function for both bosonic (blue) and fermionic (red) reheating, shown as a function of the parameter k. For bosonic reheating, the second moment increases monotonically with k, while for fermionic reheating, it approaches an asymptotic value for large k. This demonstrates that FIMPs produced during fermionic reheating carry less momentum at production than their bosonic counterparts, resulting in colder dark matter.

Figure 2.6 illustrates how the second moments of the momentum distribution function vary with the parameter k for a bosonic reheating, in blue. For bosonic reheating, we observe a clear monotonic increase in the second moment as k increases. When $k = 2$, corresponding to the early matter-dominated era, we recover the expected value $\langle q^2 \rangle |_{\mathrm{BR}}^{k=2} = 15.75$, see Sec. 2.3. As k increases to 4, the second moment rises substantially to $\langle q^2 \rangle |_{\mathrm{BR}}^{k=4} = 35.75$, indicating that FIMPs produced during bosonic reheating with higher k values carry significantly more momentum at production than those produced during the standard RD era.

2.4.3 Momentum distribution function for fermionic reheating

The derivation of the momentum distribution function for FIMPs during fermionic reheating closely follows the bosonic case. The Hubble parameter and the evolution of the inflaton energy density are also given by Eqs. (2.51) and (2.52). However, the distinct field dependence of the fermionic decay rate leads to a different expression for the radiation energy density

$$\rho_R = \frac{\sqrt{3}}{8\pi} \frac{k\sqrt{k(k-1)}}{7-k} y_{\mathrm{eff}}^2 \lambda^{1/k} M_{\mathrm{pl}}^{4/k} \rho_\phi^{\frac{k-1}{k}}(a_{\mathrm{in}}) \left[\left(\frac{a_{\mathrm{in}}}{a}\right)^{\frac{6(k-1)}{2+k}} - \left(\frac{a_{\mathrm{in}}}{a}\right)^{\frac{12(k-1)(7-k)}{2+k}} \right] \tag{2.61}$$

Figure 2.4b shows the evolution of the energy densities of the inflaton (green) and radiation (red) as a function of the scale factor, for both $k = 2$ (solid lines) and $k = 4$ (dashed lines). In contrast to the case of bosonic reheating displayed in Fig. 2.4a, we see that the reheating happens later than for $k = 2$, around $a \sim 10^{32}$, compared to $a \sim 10^{22}$ for $k = 2$. Looking at Fig. 2.3, we see the opposite behavior for fermionic reheating, meaning that now $\Gamma_\phi(k=4) < \Gamma_\phi(k=2)$ and thus $\tau_\phi(k=4) > \tau_\phi(k=2)$. It explains why the reheating happens at a later time. Thus, $\rho_R \propto a^{-\frac{6(k-1)}{2+k}}$ and $T \propto a^{-\frac{3(k-1)}{4+2k}}$, leading to

$$\xi = -\frac{3k-3}{4+2k}. \tag{2.62}$$

The radiation energy density reaches a maximum at $a_{\rm max} = a_{\rm in}\left(\frac{2k+4}{3k-3}\right)^{\frac{k+2}{14-2k}}$. We define a maximum temperature from where the temperature redshifts as

$$T = T_{\rm max}\left(\frac{a_{\rm in}}{a}\right)^{\frac{3k-3}{4+2k}}. \tag{2.63}$$

The Hubble rate in terms of temperature becomes

$$H = \frac{1}{M_0}\frac{T^{\frac{2k}{k-1}}}{T_{\rm R}^{\frac{2k}{k-1}-2}} = \frac{1}{M_0}\frac{m_B^{\frac{2k}{k-1}}}{T_{\rm R}^{\frac{2k}{k-1}-2}\,x^{\frac{2k}{k-1}}} \qquad [T_{\rm max} > T > T_R]\,. \tag{2.64}$$

Substituting into Eq. (2.14), we obtain

$$\frac{df_\chi}{dx} = \left(\frac{4+2k}{3k-3}\right)\frac{g_B\Gamma_B M_0}{m_B^2 q^2}\left(\frac{T_R}{m_B}\right)^{\frac{2k}{k-1}-2} x^{\frac{2k}{k-1}}e^{-q}e^{-\frac{x^2}{4q}}. \tag{2.65}$$

This Gaussian integral yields

$$\boxed{f(q)|_{\rm FR} = 2^{\frac{k}{k-1}}\sqrt{\pi}\,\left(\frac{k+1}{k-1}\right)!\left(\frac{4+2k}{3k-3}\right)\frac{g_B\Gamma_B M_0}{m_B^2}\left(\frac{T_R}{m_B}\right)^{\frac{2}{k-1}-2} q^{\frac{3k-5}{2k-2}}e^{-q}.} \tag{2.66}$$

Figure 2.5 also displays the momentum distribution function for fermionic reheating with $k=4$ (solid red). Similar observations to those made for bosonic reheating apply here. For fermionic reheating with $k=4$, the distribution scales at low momentum as $f(q) \propto q^{7/6}$, which is steeper than the EMD case ($f(q) \propto q^{1/2}$), but less steep than the bosonic reheating case ($f(q) \propto q^{5/2}$). This intermediate behavior is clearly visible in Fig. 2.5. At high momentum, all distributions, including that from fermionic reheating, follow the same exponential suppression, scaling as e^{-q}. The second moment of the momentum distribution function, defined by Eq. (2.23), is

$$\langle q^2\rangle\,|_{\rm FR} = \frac{\Gamma[1+\frac{13-11k}{2-2k}]}{\Gamma[1+\frac{9-7k}{2-2k}]}. \tag{2.67}$$

For fermionic reheating, Figure 2.6 reveals that the second moment increases more gradually with k, eventually approaching an asymptotic value. At $k=2$, we recover the same value as bosonic reheating, $\langle q^2\rangle\,|_{\rm FR}^{k=2} = 15.75$. However, for $k=4$, we find $\langle q^2\rangle\,|_{\rm FR}^{k=4} = 21.53$, which is considerably lower than the corresponding value for bosonic reheating ($\langle q^2\rangle\,|_{\rm BR}^{k=4} = 35.75$). This significant difference demonstrates that FIMPs produced during fermionic reheating carry less momentum at production than their bosonic counterparts, resulting in colder dark matter. This is clearly visible in the inset of Fig. 2.5, where the peak of the distribution for bosonic reheating appears at a higher value of q compared to that of fermionic reheating. It implies that FIMPs produced during bosonic reheating indeed carry more momentum at production than those produced during fermionic reheating with the same k value.

2.5 Summary of the momentum distributions in different early universe scenarios

Table 2.1 summarizes key properties of the momentum distribution function $f(q)$ for FIMPs produced via FI through decay in different early-universe scenarios. It includes the temperature dependence of the Hubble rate $H(T)$, the value of ξ, the momentum dependence of $f(q)$, and the second moment $\langle q^2 \rangle$.

Scenario	**Scaling of** $H(T)$	ξ	**Scaling of** $f(q)$	$\langle q^2 \rangle$
RD	T^2	-1	$q^{-1/2}e^{-q}$	8.75
EMD ($k = 2$)	$\frac{T^4}{T_R^2}$	$-\frac{3}{8}$	$q^{1/2}e^{-q}$	15.75
BR ($k \geq 2$)	$\frac{T^{2k}}{T_R^{2k-2}}$	$-\frac{3}{4+2k}$	$q^{k-3/2}e^{-q}$	$\frac{\Gamma[\frac{7}{2}+k]}{\Gamma[\frac{3}{2}+k]}$
FR ($k \geq 2$)	$\frac{T^{\frac{2k}{k-1}}}{T_R^{\frac{2k}{k-1}-2}}$	$-\frac{3k-3}{4+2k}$	$q^{\frac{3k-5}{2k-2}}e^{-q}$	$\frac{\Gamma[1+\frac{13-11k}{2-2k}]}{\Gamma[1+\frac{9-7k}{2-2k}]}$

Table 2.1: Summary of the momentum distribution functions and second moment for FIMPs produced in different cosmological scenarios.

Chapter 3

The comoving number density

The comoving number density is a key concept to understand the evolution of FIMP production. This quantity will let us determine the moment of the freeze-in, x_{FI}, defined as the first maximum of the comoving number density. It will also emphasize a property of reheating not yet introduced, the dilution factor. For all these reasons, this chapter is dedicated to the computation of the comoving number density of FIMP produced via the decay of a heavy mother particle, during a standard RD, EMD, and kD eras for a bosonic and fermionic reheating.
First, in Sec. 3.1, we derive the Boltzmann equation for the comoving number density. Then, we derive the comoving number density both for RD, in Sec. 3.2, and EMD eras, in Sec. 3.3. Finally, we extend the analysis to kD era for a bosonic and fermionic reheating in Sec. 3.4.

3.1 Boltzmann equation for the comoving number density

The Boltzmann equation for the comoving number density is derived from the unintegrated Boltzmann equation for the phase-space distribution, given in Eq. (1.49). To transition from the phase-space distribution to the number density, we use the definition

$$n_\chi(x) = \int \frac{d^3p}{(2\pi)^3} f_\chi(x,p). \tag{3.1}$$

Integrating both sides of Eq. (1.49) over momentum then yields the Boltzmann equation governing the evolution of the number density

$$\dot{n}_\chi + 3Hn_\chi = \int \frac{d^3p_\chi}{(2\pi)^3 2E_\chi}\mathcal{C}[f_\chi]. \tag{3.2}$$

The right-hand side is obtained by applying the same assumptions as in Sec. 2.1, namely that χ is produced via the decay of a heavy mother particle B in thermal and chemical equilibrium with the bath, considered non-relativistic, and that spin-statistic effects can be neglected. Under these conditions, the collision term simplifies to

$$\int \frac{d^3p_\chi}{(2\pi)^3 2E_\chi}\mathcal{C}[f_\chi] = n_B^{\mathrm{eq}}\Gamma_B \frac{K_1[m_B/T]}{K_2[m_B/T]}, \tag{3.3}$$

where $K_{1,2}$ are the modified Bessel functions of the first and second kind, and n_B^{eq} the equilibrium number density of the mother particle, given by

$$n_B^{\mathrm{eq}} = g_B \int \frac{d^3p}{(2\pi)^3} f_B^{\mathrm{eq}} = \frac{g_B}{2\pi^2} m_B^2 T K_2[m_B/T]. \tag{3.4}$$

Substituting the expression for the collision term into Eq. (3.2), we obtain the Boltzmann equation for the number density [18, 20, 36].

$$\dot{n}_\chi + 3Hn_\chi = n_B^{\text{eq}}\Gamma_B \frac{K_1[m_B/T]}{K_2[m_B/T]}. \tag{3.5}$$

In the following section, we solve this equation in RD era before going to non-standard cosmologies.

3.2 Radiation-dominated era

In this section we solve the Boltzmann equation for the number density, given by Eq. (3.5), for FIMP produced during a RD era. To factor out the effect of expansion, it is convenient to introduce the comoving number density

$$Y_\chi = \frac{n_\chi}{s}, \tag{3.6}$$

where s is the entropy density. For radiation, it is defined as

$$s(T) = \frac{2\pi^2}{45} g_{\star s}(T)T^3, \tag{3.7}$$

where $g_{\star s}$ represents the effective relativistic degrees of freedom for entropy

$$g_{\star s}(T) = \sum_{\text{bosons}} g_i \left(\frac{T_i}{T}\right)^3 + \frac{7}{8}\sum_{\text{fermions}} g_i \left(\frac{T_i}{T}\right)^3. \tag{3.8}$$

The comoving number density remains constant under adiabatic expansion in absence of processes changing the number of particles, since both the number density and the entropy density scale as a^{-3} [18, 20]. Introducing this variable and changing the time derivative to a derivative with respect to $x = m_B/T$, Eq. (3.5) becomes

$$\frac{dY_\chi}{d\ln x} = \frac{1}{H(x)} Y_B^{\text{eq}}\Gamma_B \frac{K_1[x]}{K_2[x]}. \tag{3.9}$$

Substituting the expression for the Hubble rate in RD era, given by Eq. (2.18), we obtain

$$\frac{dY_\chi}{d\ln x} = \frac{M_0\Gamma_B}{m_B^2} Y_B^{\text{eq}} x^2 \frac{K_1[x]}{K_2[x]}. \tag{3.10}$$

This equation can be solved numerically to obtain the evolution of the comoving number density. The solution is shown in Fig. 1.4 for different values of the decay width Γ_B. To better understand the behavior of the comoving number density, we refer to the approximate solution obtained from the rule-of-thumb argument, Eq. (1.9), which reads

$$Y_\chi(x) \simeq \frac{\Gamma_B M_{\text{pl}}}{m_B^2} x^3. \tag{3.11}$$

This expression shows the IR domination of the freeze-in process mentioned in Sec. 1.1.2, as it shows that the comoving number density increases with decreasing temperature, i.e., increasing

x. It also illustrates the dependence of the FIMP comoving number density on the properties of the mother particle: a larger m_B leads to a lower FIMP abundance, while a larger decay rate Γ_B results in a higher abundance, as illustrated in Fig. 1.4. However, this approximation is only valid while the abundance of the mother particle B remains high, i.e., for $x < 3$. At this point, freeze-in occurs, and beyond $x = 3$, $H > Y_B^{\rm eq}\Gamma_B$, and the abundance of B becomes Boltzmann suppressed. As a result, Y_χ reaches a constant asymptotic value, $Y_\chi^\infty = Y_\chi(x_{\rm FI})$. Using our expression for $Y_\chi(x)$ and that $x_{\rm FI} \simeq 3$, we find

$$Y_\chi^\infty \simeq 10\frac{\Gamma_B M_0}{m_B^2}. \tag{3.12}$$

Rigorously, this value is obtained by integrating Eq. (3.10) analytically from 0 to ∞, assuming that the initial number density of FIMP is zero [20]. This asymptotic value corresponds to the total comoving abundance of χ particles produced through the freeze-in mechanism. From this result, the relic density today is given by

$$\Omega_\chi h^2 = \frac{m_\chi Y_\chi^\infty s_0}{\rho_{\rm crit}/h^2} \simeq 10\frac{\Gamma_B M_0}{m_B^2}\frac{m_\chi s_0}{\rho_{\rm crit}/h^2}, \tag{3.13}$$

where s_0 is the entropy density today [18, 20, 22]. This result matches the estimate obtained using the rule-of-thumb approach discussed in Sec. 1.1.2. It allows us to place constraints on the properties of both the mother particle B and the FIMP by requiring consistency with the observed dark matter abundance, assuming that FIMPs account for all the dark matter, $\Omega_\chi h^2 \approx 0.12$.

3.3 Early matter-dominated era

We now solve Eq. (3.5) for FIMPs produced during an early matter-dominated era. In this case, FI occurs before the end of reheating, at a temperature $T_{\rm FI} > T_R$. During the reheating period, entropy is not conserved due to the decay of the inflaton into radiation. Consequently, the comoving number density is diluted for $T_{\rm FI} > T > T_R$. Even in the absence of any processes that change the number of particles, the comoving number density Y_χ does not remain constant but decreases due to this entropy injection. To better describe the evolution of the number density in this regime, we introduce a new variable

$$\mathcal{X} = n_\chi a^{-3}. \tag{3.14}$$

which has an analogous role as Y_χ in RD, it remains constant after freeze-in occurs. Substituting this variable and changing the time derivative to a derivative with respect to the scale factor, Eq. (3.5) becomes

$$\frac{d\mathcal{X}}{d\ln a} = \frac{a^3}{H(a)} n_B^{\rm eq}\Gamma_B \frac{K_1\left[\frac{m_B}{T}\right]}{K_2\left[\frac{m_B}{T}\right]}. \tag{3.15}$$

This equation can be solved numerically using the Friedmann equation for H, Eq. (1.38), together with the coupled Boltzmann equations for ρ_ϕ and ρ_R, given by Eqs. (2.25) and (2.26) [20]. The numerical results are presented in Fig. 3.1, which shows the comoving number density of the FIMP as a function of x. The dashed purple curve represents the solution for the RD era, while the solid lines correspond to the EMD era, with reheating temperatures

$T_R = 25$ GeV (blue), $T_R = 100$ GeV (red) and $T_R = 100$ TeV (green). We observe that the location of the first maximum of Y_χ differs between the RD (vertical dashed line) and EMD (vertical long-dashed line) eras. This maximum indicates the moment of freeze-in, which occurs at $x_{\rm FI}|_{\rm EMD} \simeq 6$, compared to $x_{\rm FI}|_{\rm RD} \simeq 3$. Therefore, freeze-in happens at a lower temperature in the EMD era. Taking $m_B = 1$ TeV, the corresponding freeze-in temperature is

$$T_{\rm FI} = \left(\frac{m_B}{1\ \text{TeV}}\right)\left(\frac{x_{\rm FI}}{6}\right)^{-1}. \tag{3.16}$$

For $T_R = 100$ TeV, we observe a change in the slope that signals the transition from an EMD era to a RD era. However, this transition occurs before freeze-in takes place, and thus it does not impact the final yield. This explains why, in Fig. 2.1, the curve corresponding to $T_R = 500$ GeV shows a slight deviation at low q, yet ultimately results in the same relic density.
To understand the physics behind the curves in Fig. 3.1, we consider the approximate solution Eq. (1.8) for the EMD era [20]. Using the Hubble rate derived in Eq. (2.29), the approximate production of $Y_\chi = \mathcal{X}/S$, for $x < 6$, is

$$Y_\chi(x) \simeq \frac{\Gamma_B \tilde{M}_0}{m_B^2}\left(\frac{T_R}{m_B}\right)^2 x^5. \tag{3.17}$$

This expression exhibits an explicit dependence on the reheating temperature, with $Y_\chi \propto T_R^2$. A higher reheating temperature therefore leads to a larger FIMP abundance, which explains the difference between the blue and red curves in Fig 3.1. Moreover, the scaling $Y_\chi^{\rm EMD} \propto x^5$, in the EMD era differs from $Y_\chi^{\rm RD} \propto x^3$ in the RD era, which accounts for the steeper slope of the EMD production curves, shown in Fig. 3.1.
We cannot estimate Y_χ^∞ directly from $Y_\chi(x_{\rm FI})$, because the number density is diluted between $T_{\rm FI}$ and T_R. This explains the drop observed in Fig. 3.1 after the production peak, before reaching the final plateau, unlike in the RD case, where the plateau is reached immediately after freeze-in. We quantify this dilution with the ratio of the entropy at temperature T to the entropy at the reheating temperature

$$D(T) = \frac{S(T)}{S(T_R)} = \frac{s(T)a^3(T)}{s(T_R)a^3(T_R)} \qquad [T_{\max} > T > T_R]\,. \tag{3.18}$$

From the relation between the temperature and the scale factor in the EMD era, Eq. (2.31), we deduce

$$D(T) = \left(\frac{T_R}{T}\right)^5 \tag{3.19}$$

Taking this dilution into account, we define the effective comoving number density

$$\tilde{Y}_\chi(x) = Y_\chi(x)D(x) \simeq \frac{\Gamma_B \tilde{M}_0}{m_B^2}\left(\frac{T_R}{m_B}\right)^7 x^{10}. \tag{3.20}$$

This shows that the process is extremely IR dominated [20]. Using this expression and the moment of the FI, $x_{\rm FI} \simeq 6$, we estimate the asymptotic comoving number density as

$$\tilde{Y}_\chi^\infty \simeq 10^7 \left(\frac{T_R}{m_B}\right)^7 \frac{\Gamma_B \tilde{M}_0}{m_B^2}. \tag{3.21}$$

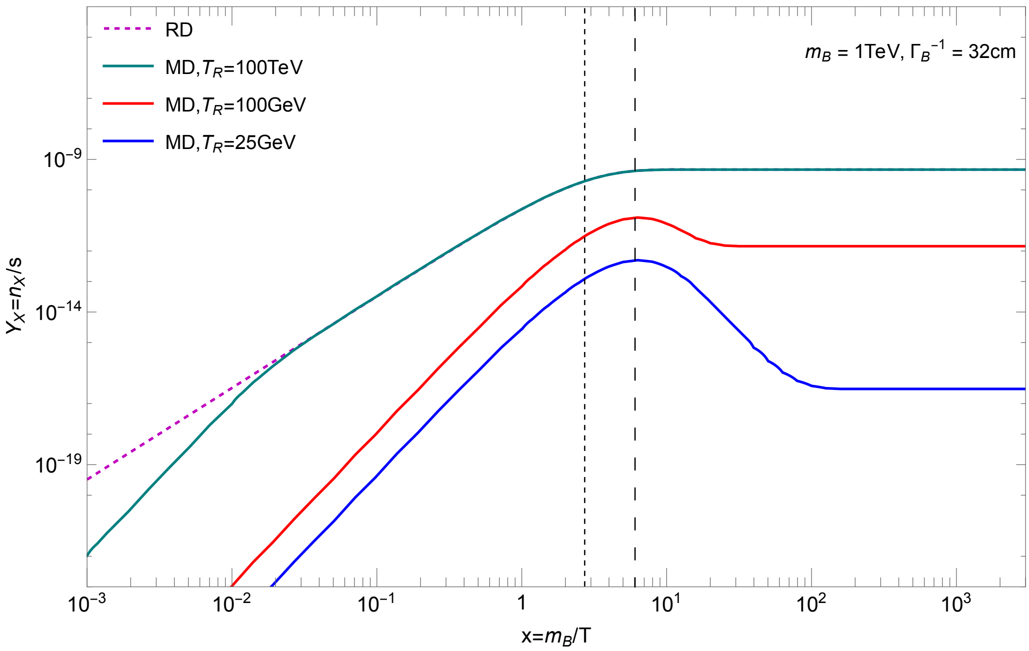

Figure 3.1: Log-log plot of the comoving number density Y_χ as a function of $x = m_B/T$ for FIMPs with $m_B = 1$ TeV produced during RD (purple dashed) and EMD eras with $T_R = 25$ GeV (blue), $T_R = 100$ GeV (red) and $T_R = 100$ TeV (green). The vertical dashed lines indicate the freeze-in temperature for RD ($x_{\rm FI} \simeq 3$) and EMD ($x_{\rm FI} \simeq 6$) eras. The decrease in the red and blue curves illustrates the entropy dilution effect absent in standard cosmology.

Compared to the RD era, the final abundance is suppressed by a factor $(T_R/m_B)^7$, which explains the several orders of magnitude difference seen in Fig. 3.1. We use this estimation to compute the relic density

$$\Omega_\chi h^2 = \frac{m_\chi \tilde{Y}_\chi^\infty s_0}{\rho_{\rm crit}/h^2} \simeq 10^7 \left(\frac{T_R}{m_B}\right)^7 \frac{\Gamma_B \tilde{M}_0}{m_B^2} \frac{m_\chi s_0}{\rho_{\rm crit}/h^2}. \tag{3.22}$$

The same suppression factor affects the relic density of FIMP today. Consequently, the constraints on the properties of the mother particle and the FIMP, derived by imposing $\Omega_\chi h^2 \approx 0.12$, are reduced by this factor. This leads to an interesting outcome: it allows for heavier FIMPs while still permitting the mother particle to decay within the detector of a collider experiment [20].

3.4 Early k-dominated era

The derivation of the comoving number density of FIMPs during an early matter-dominated era can be extended to an early cosmology characterized by a monomial inflaton potential, parametrized by the value k, with $2 < k < 7$. As discussed in Sec. 2.4.1, obtaining a general result requires specifying the reheating mechanism that is responsible for the transitions to the radiation-dominated era. In this section, we consider both bosonic and fermionic reheating scenarios and derive the evolution of the FIMP comoving number density produced during reheating with $2 < k < 7$.

As in the EMD case, the evolution of the comoving number density is governed by the Boltzmann equation

$$\frac{d\mathcal{X}}{d\ln a} = \frac{a^3}{H(a)} n_B^{\rm eq} \Gamma_B \frac{K_1\left[\frac{m_B}{T}\right]}{K_2\left[\frac{m_B}{T}\right]}, \tag{3.23}$$

where $\mathcal{X} = na^3$ and H is obtained from the Friedmann equation, Eq. (1.38), using the energy densities of inflaton given by Eq. (2.49) and radiation given by Eq. (2.50) for bosonic reheating, and Eq. (2.61) for fermionic reheating. The comoving number density is then defined as

$$Y(T) = \frac{\mathcal{X}(T)}{S(T)}. \tag{3.24}$$

To better understand the distinct features of the two reheating scenarios, we derive approximate expressions for Y_χ. Starting from Eq. (1.8) and using the Hubble rates for each case, Eqs. (2.57) and (2.64), we obtain

$$Y_\chi(x) \simeq \frac{\Gamma_B M_0}{m_B^2}\left(\frac{T_R}{m_B}\right)^{2k-2} x^{2k+1}, \qquad \text{BR} \tag{3.25}$$

$$Y_\chi(x) \simeq \frac{\Gamma_B M_0}{m_B^2}\left(\frac{T_R}{m_B}\right)^{\frac{2}{k-1}} x^{\frac{3k-1}{k-1}}, \qquad \text{FR} \tag{3.26}$$

in agreement with [38]. We observe that for bosonic reheating, the power of x increases with k, leading to steeper production for higher k. In contrast, the exponent in the fermionic case decreases with increasing k, indicating a more gradual production. However, the dilution of the comoving number density due to entropy production during reheating must also be taken into account [38]. Using the relations between T and a given by Eq. (2.56) for bosonic reheating and Eq. (2.63) for fermionic reheating, the dilution factor is, for $T_{\rm max} > T > T_R$,

$$D(T,k) = \left(\frac{T_R}{T}\right)^{1+2k}, \qquad \text{BR} \tag{3.27}$$

$$D(T,k) = \left(\frac{T_R}{T}\right)^{\frac{7-k}{k-1}}. \qquad \text{FR} \tag{3.28}$$

These relations lead to distinctive behaviors between bosonic and fermionic reheating. For bosonic reheating, the exponent $(1+2k)$ increases monotonically with k, leading to stronger dilution at higher k. However, for fermionic reheating, the exponent $\frac{7-k}{k-1}$ decreases with increasing k, resulting in weaker dilution at higher k. Including this effect, the approximate comoving number densities become [38]

$$\tilde{Y}_\chi(x) \simeq \frac{\Gamma_B M_0}{m_B^2}\left(\frac{T_R}{m_B}\right)^{4k-1} x^{4k+2}, \qquad \text{BR} \tag{3.29}$$

$$\tilde{Y}_\chi(x) \simeq \frac{\Gamma_B M_0}{m_B^2}\left(\frac{T_R}{m_B}\right)^{\frac{9-k}{k-1}} x^{\frac{2k+6}{k-1}}. \qquad \text{FR} \tag{3.30}$$

These expressions show that bosonic reheating leads to a stronger suppression of the comoving number density due to entropy dilution as k increases than in the RD case for $T_R < T_{\rm FI}$. Additionally, the dependence on x becomes steeper with increasing k. In contrast, for fermionic reheating, the dilution factor weakens as k increases, resulting in a less suppressed comoving

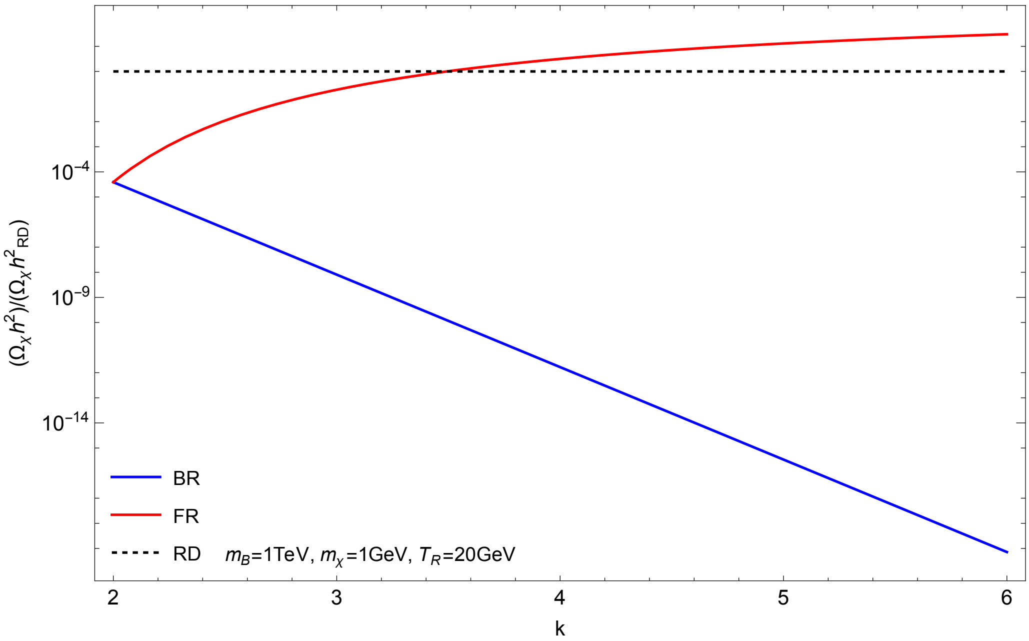

Figure 3.2: Relic abundance of FIMPs, $\Omega_\chi h^2$, produced during bosonic (blue) and fermionic (red) reheating as a function of the parameter k, for a fixed mother particle mass $m_B = 1$ TeV and FIMP mass $m_\chi = 1$ GeV, and a reheating temperature $T_R = 20$ GeV. The black dashed line corresponds to the standard RD era. The two scenarios show opposite behavior with increasing k.

number density for larger values of k. In both cases, setting $k = 2$ reproduces the result obtained in the EMD era, as given in Eq. (3.20).
Since FIMP production is most efficient near $x_{\rm FI}$, the relic abundance today is given by

$$\Omega_\chi h^2 \simeq x_{\rm FI}^{4k+2} \left(\frac{T_R}{m_B}\right)^{4k-1} \Omega_\chi h^2|_{\rm RD}, \qquad \text{BR} \tag{3.31}$$

$$\Omega_\chi h^2 \simeq x_{\rm FI}^{\frac{2k+6}{k-1}} \left(\frac{T_R}{m_B}\right)^{\frac{9-k}{k-1}} \Omega_\chi h^2|_{\rm RD}, \qquad \text{FR} \tag{3.32}$$

where $\Omega_\chi h^2|_{\rm RD}$ is given by Eq. (3.13). The resulting relic densities, using $x_{\rm FI} = 6$ for illustration, are plotted in Fig. 3.2 for bosonic reheating (solid blue), fermionic reheating (solid red), and the standard RD case (black dashed). We observe that, in bosonic reheating, the relic density is suppressed relative to the RD value by a factor $(T_R/m_B)^{4k-1}$. In contrast, for fermionic reheating, the relic density grows slowly with k.

3.5 Summary of comoving number density properties in different early universe scenarios

Table 3.1 summarizes key properties of the comoving number density $\tilde{Y}_\chi(x)$ for FIMPs produced via freeze-in from decays in different early-universe scenarios. The table includes the scaling of $\tilde{Y}_\chi$ with x, the entropy dilution factor, and the moment of the freeze-in where the production of FIMP is suppressed.

Scenario	**Scaling of $\tilde{Y}_\chi(x)$**	**Dilution Factor**	$x_{\mathbf{FI}}$
RD	x^3	1	∼3
EMD ($k = 2$)	$\left(\frac{T_R}{m_B}\right)^7 x^{10}$	$\left(\frac{T_R}{T}\right)^5$	∼6
BR ($k \geq 2$)	$\left(\frac{T_R}{m_B}\right)^{4k-1} x^{4k+2}$	$\left(\frac{T_R}{T}\right)^{1+2k}$	∼6-10
FR ($k \geq 2$)	$\left(\frac{T_R}{m_B}\right)^{\frac{9-k}{k-1}} x^{\frac{2k+6}{k-1}}$	$\left(\frac{T_R}{T}\right)^{\frac{7-k}{k-1}}$	∼6-10

Table 3.1: Comparison of FIMP production characteristics across different cosmological scenarios.

Chapter 4

The Lyman-α constraints

In this final chapter, we focus on the constraints on FIMPs produced during a reheating period. In particular, we derive the Lyman-α constraints in both RD and kD eras. To achieve this, we reinterpret the existing constraints on WDM into FIMPs for the different early universe scenarios.
We begin in Sec. 4.1 by developing the method for comparing the velocity dispersion of FIMPs with that of warm dark matter. Then, in Sec. 4.2, we derive the Lyman-α constraints for FIMPs produced during a RD era. In Sec. 4.3, we proceed with the computation of the constraints in an EMD era. Finally, in Sec. 4.4, we present the Lyman-α constraints in a kD era, for both bosonic and fermionic reheating scenarios.

4.1 Velocity dispersion method

In Sec. 1.1.3, we saw that the mass of warm dark matter (WDM) is constrained by Lyman-α, yielding the lower bound [27]

$$m_{\mathrm{WDM}}^{\mathrm{Ly}\alpha} \geq 5.3 \text{ keV}. \tag{4.1}$$

This constraint is derived from expansive hydrodynamical simulations. Rather than repeating this analysis for FIMPs, we can transpose the Lyman-α bound from WDM to FIMP. Several methods to do so are discussed in [19]. Both WDM and FIMP belong to the category of non-cold dark matter, meaning their velocity dispersions at the time of production are non-negligible. The velocity dispersion of a dark matter particle X is defined as

$$\sigma^X = \frac{\sqrt{\langle p^2 \rangle_X}}{m_X}, \tag{4.2}$$

where it depends on the second moment of the momentum distribution function of X and its mass. We can constrain FIMPs from FI through the decays of a heavy particle by requiring that their velocity dispersion today is no greater than that of WDM constrained by Lyman-α [19]

$$\sigma_0^{\mathrm{FIMP}} \leq \sigma_0^{\mathrm{WDM}}|_{\mathrm{Ly}\alpha}. \tag{4.3}$$

To proceed, we compute the velocity dispersions for both FIMP and WDM. In Chapter 2, we derived the FIMP momentum distribution function $f(q)$ at the time of freeze-in using the variables $x = m_B/T$ and $q = p/T$. Hence, we aim to express both WDM and FIMP velocity dispersions in terms of these variables at the time of production.

We begin with the velocity dispersion of WDM, which is given by

$$\sigma_0^{\rm WDM} = \frac{\sqrt{\langle p^2\rangle_0^{\rm WDM}}}{m_{\rm WDM}}. \tag{4.4}$$

To compute the second moment at the present time, we use that momenta redshift as $1/a$ due to the expansion of the Universe

$$\sqrt{\langle p^2\rangle_0^{\rm WDM}} = \sqrt{\langle p^2\rangle_{\rm FD}^{\rm WDM}}\frac{a_{\rm WDM}}{a_0}\frac{T_{\rm WDM}}{T_{\rm WDM}} = \sqrt{\langle q^2\rangle_{\rm FD}^{\rm WDM}}\frac{a_{\rm WDM}}{a_0}T_{\rm WDM}, \tag{4.5}$$

with $T_{\rm WDM}$ the temperature of WDM at the time of production. We inserted the identity $T_{\rm WDM}/T_{\rm WDM}$ to make the variable q appear explicitly. Using entropy conservation, we relate the production temperature to today's temperature

$$T_{\rm WDM} = \left(\frac{g_{\star s}(T_0)}{g_{\star s}(T_{\rm WDM})}\right)^{1/3}\frac{a_0}{a_{\rm WDM}}T_0, \tag{4.6}$$

where the ratio of $g_{\star s}$ arises assuming entropy conservation between T_0 and $T_{\rm WDM}$. For thermal WDM, which was in equilibrium with the thermal bath, its phase space distribution is either Fermi-Dirac or Bose-Einstein. Its present-day energy density is given by $\rho_{\rm WDM} = n_{\rm WDM}m_{\rm WDM}$, and the relic abundance obtained through relativistic freeze-out reads

$$\Omega_{\rm WDM}h^2 = \frac{m_{\rm WDM}}{94\ {\rm eV}}\left(\frac{T_{{\rm WDM},0}}{T_{\nu,0}}\right)^3 = 7.5\left(\frac{m_{\rm WDM}}{7\ {\rm keV}}\right)\left(\frac{106.75}{g_\star(T_{\rm WDM})}\right), \tag{4.7}$$

where $T_{\nu,0}$ is the temperature of the neutrino today and $T_{{\rm WDM},0}$ is the temperature of WDM today [44, 45]. In the second equality, we used entropy conservation. Assuming WDM constitutes all the dark matter, i.e., $\Omega_{\rm WDM}h^2 = 0.12$, we find

$$g_\star(T_{\rm WDM}) = 953.125\left(\frac{m_{\rm WDM}}{\rm keV}\right). \tag{4.8}$$

Substituting this into Eq. (4.6) and plugging the result into Eq. (4.5), we obtain

$$\sqrt{\langle p^2\rangle_0^{\rm WDM}} = 0.001\sqrt{\langle q^2\rangle_{\rm FD}^{\rm WDM}}\,g_{\star s}(T_0)^{1/3}\left(\frac{\rm keV}{m_{\rm WDM}}\right)^{1/3}T_0, \tag{4.9}$$

where $\langle q^2\rangle_{\rm FD}^{\rm WDM}$ is the second moment of the FD distribution. Thus, the velocity dispersion of WDM today becomes [19, 44, 45]

$$\sigma_0^{\rm WDM} = 0.001\sqrt{\langle q^2\rangle_{\rm FD}^{\rm WDM}}\,g_{\star s}(T_0)^{1/3}\left(\frac{\rm keV}{m_{\rm WDM}}\right)^{4/3}T_0, \tag{4.10}$$

where $\sqrt{\langle q^2\rangle_{\rm FD}^{\rm WDM}} \simeq 3$. In the following sections, we derive the velocity dispersion of FIMPs produced during RD, EMD, and kD eras. We then compare these results to the velocity dispersion of WDM to interpret the Lyman-α constraints into bounds on FIMPs.

4.2 Radiation-dominated era

We now turn to the computation of the velocity dispersion of FIMPs produced during RD era. To do so, we calculate the second moment of the momentum distribution function at the time of freeze-in. As in the case of WDM discussed in the previous section, the velocity dispersion today corresponds to the redshifted value of the distribution at the time of FI

$$\sqrt{\langle p^2\rangle_0^{\mathrm{RD}}} = \sqrt{\langle q^2\rangle_{\mathrm{FI}}^{\mathrm{RD}}}\frac{a_{\mathrm{FI}}}{a_0}T_{\mathrm{FI}}. \tag{4.11}$$

Using entropy conservation, we relate the FI temperature to the temperature today

$$T_{\mathrm{FI}} = \left(\frac{g_{\star s}(T_0)}{g_{\star s}(T_{\mathrm{FI}})}\right)^{1/3}\frac{a_0}{a_{\mathrm{FI}}}T_0 \tag{4.12}$$

Combining these results, the velocity dispersion of FIMPs produced in the RD era becomes

$$\sigma_0^{\mathrm{RD}} = \frac{\sqrt{\langle q^2\rangle_{\mathrm{FI}}^{\mathrm{RD}}}}{m_{\chi,\mathrm{RD}}}\left(\frac{g_{\star s}(T_0)}{g_{\star s}(T_{\mathrm{FI}})}\right)^{1/3}T_0. \tag{4.13}$$

We compare this to the velocity dispersion of WDM, given in Eq. (4.10), and apply the Lyman-α bound on WDM, which leads to the constraint

$$m_{\chi,\mathrm{RD}} \geq 0.7\ \mathrm{keV}\sqrt{\langle q^2\rangle_{\mathrm{FI}}^{\mathrm{RD}}}\left(\frac{m_{\mathrm{WDM}}^{\text{Ly-}\alpha}}{\mathrm{keV}}\right)^{4/3}. \tag{4.14}$$

This constraint depends on the second moment of the FIMP momentum distribution, which is given by Eq. (2.24). We then find the Lyman-α bound for FIMPs produced during the RD era

$$m_{\chi,\mathrm{RD}} \geq 16\ \mathrm{keV}\left(\frac{m_{\mathrm{WDM}}^{\mathrm{Ly}\alpha}}{5.3\ \mathrm{keV}}\right)^{4/3}. \tag{4.15}$$

In agreement with [19]. We now turn to the case where FIMPs are produced during an EMD era. In this scenario, both the second moment of the momentum distribution function and the entropy evolution differ significantly from the RD case, leading to a modified velocity dispersion today.

4.3 Early matter-dominated era

In this section we compute the velocity dispersion of FIMP produced during an early matter-dominated era. As before, the second moment of the momentum distribution today is redshifted to its value at the time of FI,

$$\sqrt{\langle p^2\rangle_0^{\mathrm{EMD}}} = \sqrt{\langle q^2\rangle_{\mathrm{FI}}^{\mathrm{EMD}}}\frac{a_{\mathrm{FI}}}{a_0}T_{\mathrm{FI}}. \tag{4.16}$$

However, in this case entropy is not conserved for $T_{\mathrm{FI}} > T > T_R$, so we must proceed differently. We begin by rewriting the factor

$$\frac{(aT)|_{\mathrm{FI}}}{(aT)|_0} = \frac{(aT)|_{\mathrm{Fi}}}{(aT)|_R}\frac{(aT)|_R}{(aT)|_0} = D(T_{\mathrm{FI}})^{1/3}\left(\frac{g_{\star s}(T_0)}{g_{\star s}(T_{\mathrm{FI}})}\right)^{1/3}. \tag{4.17}$$

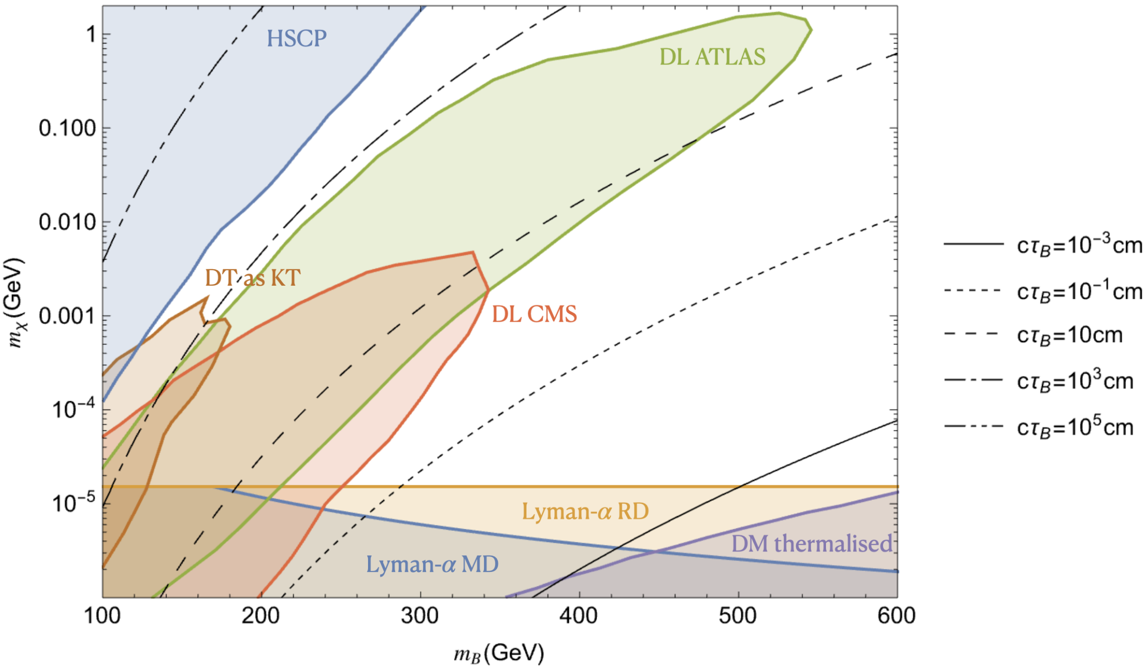

Figure 4.1: Collider and Lyman-α constraints on FIMP produced during an EMD era, shown in the (m_B, m_χ) plane. The colored regions show excluded parameter space. The collider constraints, derived under a leptophilic scenario, are taken from [20]. The Lyman-α constraints for RD (orange) and EMD (blue) eras have been computed in Chapter 4. The black dashed lines indicate values of the mother particle decay width that yield a present-day FIMP relic density of $\Omega_\chi h^2 = 0.12$.

We have split the ratio into two parts: the evolution from FI to reheating, and from reheating to today. The second part is straightforward, since after reheating the universe returns to a radiation-dominated phase where entropy is conserved. This gives the usual ratio of entropy degrees of freedom. The first term corresponds to the ratio of entropies at freeze-in and reheating, raised to the one-third power, which is the definition of the dilution factor $D(T_{\rm FI})$ from Eq. (3.18). Substituting this into Eq. (4.16) yields the velocity dispersion

$$\sigma_0^{\rm EMD} = \frac{\sqrt{\langle q^2 \rangle_{\rm FI}^{\rm EMD}}}{m_{\chi,\rm EMD}} D(T_{\rm FI})^{1/3} \left(\frac{g_{\star s}(T_0)}{g_{\star s}(T_{\rm FI})}\right)^{1/3} T_0. \tag{4.18}$$

Comparing this to the WDM velocity dispersion, we obtain the Lyman-α bound

$$\boxed{m_{\chi,\rm EMD} \geq 0.7\ {\rm keV} \sqrt{\langle q^2 \rangle_{\rm FI}^{\rm EMD}} \left(\frac{T_R x_{\rm FI}}{m_B}\right)^{5/3} \left(\frac{m_{\rm WDM}^{\text{Ly-}\alpha}}{\rm keV}\right)^{4/3},} \tag{4.19}$$

where we used the expression for the dilution factor from Eq. (3.19). This represents the Lyman-α constraint on FIMPs produced during an EMD era. Compared to the RD case, the differences lie in the second moment of the momentum distribution function, given by Eq. (2.38) in EMD and Eq. (2.24) in RD era, and the appearance of the dilution factor.
In Fig. 4.1, we show the Lyman-α constraint in the EMD case, along with CMS and ATLAS bounds from [20], in the (m_B, m_χ) plane for $T_R = 20$ GeV. We observe that the constraint

weakens as m_B increases. This behavior arises from the dilution factor at the FI temperature. The FI temperature is determined by the moment of the FI, typically around $x_{\rm FI} \sim 6$, as discussed in Sec. 3.3, and the mass of the mother particle, $T_{\rm FI} = m_B/x_{\rm FI}$. As m_B increases, so does $T_{\rm FI}$, which implies a longer duration between freeze-in and reheating. This extended period allows for more dilution of the FIMP abundance, thereby weakening the constraints. Furthermore, for a fixed m_B, increasing the reheating temperature reduces the time available for dilution, resulting in a stronger constraint. For instance, at $T_R = 20$ GeV and $m_B = 200$ GeV, considering $m_{\rm WDM}^{\rm Ly\alpha} = 5.3$ keV, the constraint becomes $m_\chi \geq 11.84$ keV. This can be compared to the RD case, where the constraint is independent of the mass of the mother particle and gives $m_\chi \geq 16$ keV. Additionally, Fig. 4.1 shows that for $m_B \leq 120$ GeV, the constraints in both the EMD and RD eras coincide. This occurs because, for such values of m_B, the freeze-in temperature satisfies $T_{\rm FI} < T_R$, implying that the production of FIMPs takes place during the RD era. Consequently, we recover the standard RD constraint. Dashed black contours in the Fig. 4.1, indicate the decay width of the mother particle that lead to the observed dark matter abundance today, assuming FIMPs constitute all the dark matter, i.e., $\Omega_{\rm FIMP}h^2 = 0.12$.
The remaining constraints in Fig. 4.1, taken from Calibbi *et al.* [20], arise from CMS and ATLAS searches for various collider signatures, as discussed in Sec. 1.1.3. These signals are model-dependent. Calibbi *et al.* consider a leptophilic scenario in which the mother particle is a scalar ϕ_B, carrying an electric charge, and the FIMP is a Majorana fermion singlet χ, both coupling only to right-handed muons. The relevant terms in the Lagrangian are

$$L_{\rm lepto} \supset \frac{1}{2}\bar{\chi}\gamma^\mu\partial_\mu\chi - \frac{m_\chi}{2}\bar{\chi}\chi + (D_\mu\phi_B)^\dagger D^\mu\phi_B - m_{\phi_B}^2|\phi_B|^2 - \kappa\phi_B\bar{\chi}\mu_R + h.c., \tag{4.20}$$

where κ is a dimensionless Yukawa coupling. The charged scalar ϕ_B can be pair-produced at colliders, and depending on its decay rate, gives rise to distinct signals such as displaced leptons (DL), disappearing or kinked tracks (DT/KT), and heavy stable charged particles (HSCP), as discussed in [20].

4.4 Early k-dominated era

In this section we compute the Lyman-α constraints on FIMP produced during a reheating period parametrized by k, which defines the power of the monomial inflaton potential. We investigate both bosonic and fermionic reheating scenarios.
The method we employ is the same as for the EMD era. First, we express the second moment at the freeze-in temperature. Then, we describe the ratio of aT in terms of the dilution factor $D(T_{\rm FI}, k)$ and the ratio of effective degrees of freedom. This leads to the following expressions for the velocity dispersion of FIMPs produced during bosonic and fermionic reheating

$$\sigma_0^\Upsilon = \frac{\sqrt{\langle q^2\rangle_{\rm FI}^\Upsilon}}{m_{\chi,\Upsilon}} D_\Upsilon(T_{\rm FI}, k)^{1/3}\left(\frac{g_{\star s}(T_0)}{g_{\star s}(T_{\rm FI})}\right)^{1/3} T_0, \tag{4.21}$$

where $\Upsilon = $ BR or FR, and $D_\Upsilon(T_{\rm FI}, k)$ is the dilution factor given by Eq. (3.27) for bosonic reheating and Eq. (3.28) for fermionic reheating. The two scenarios differ for $2 < k < 7$ due to the different k-dependence of their second momenta and dilution factors, see Secs. 2.4.3 and

2.4.2. It leads to the Lyman-α constraints for FIMPs produced during bosonic reheating

$$\boxed{m_{\chi,\mathrm{BR}} \geq 0.7\ \mathrm{keV}\sqrt{\langle q^2\rangle_{\mathrm{FI}}^{\mathrm{BR}}}\left(\frac{T_R x_{\mathrm{FI}}}{m_B}\right)^{\frac{1+2k}{3}}\left(\frac{m_{\mathrm{WDM}}^{\text{Ly-}\alpha}}{\mathrm{keV}}\right)^{4/3},} \tag{4.22}$$

and during fermionic reheating

$$\boxed{m_{\chi,\mathrm{FR}} \geq 0.7\ \mathrm{keV}\sqrt{\langle q^2\rangle_{\mathrm{FI}}^{\mathrm{FR}}}\left(\frac{T_R x_{\mathrm{FI}}}{m_B}\right)^{\frac{7-k}{3k-3}}\left(\frac{m_{\mathrm{WDM}}^{\text{Ly-}\alpha}}{\mathrm{keV}}\right)^{4/3}.} \tag{4.23}$$

In Figs. 4.2a and 4.2b, we show the Lyman-α constraints on FIMPs produced via the decay of a heavy mother particle B during bosonic (a) and fermionic (b) reheating in the $(k, T_R/m_B)$ parameter space. The lower bound on the FIMP mass, $m_\chi^{\mathrm{Ly}\alpha}$, which saturates Eqs. 4.22 and 4.23, is indicated by a color gradient, with red representing stronger bounds and blue weaker ones. The maximum value of T_R/m_B shown on the plots is 0.16, corresponding to $T_R = T_{\mathrm{FI}}$ with $x_{\mathrm{FI}} = 6$. Beyond this point, FIMPs are produced during a radiation-dominated era, and the constraints reduce to the standard RD given by Eq. (4.15).

In Fig. 4.2a (bosonic reheating), we observe that the Lyman-α constraints become stronger for larger reheating temperatures T_R, and weaker for higher values of the parameter k for $T_R \ll T_{\mathrm{FI}}$. This behavior arises from the dilution factor that enters the Lyman-α constraints, which scale as $m_{\chi,\mathrm{BR}} \propto (T_R x_{\mathrm{FI}}/m_B)^{\frac{1+2k}{3}}$. For fixed values of k and m_B, increasing T_R reduces the time available for dilution, thereby leading to stronger constraints. The exponent $\frac{1+2k}{3}$ is positive and increases with k for $k \geq 2$, so for a fixed T_R and m_B, increasing k enhances the dilution and thus weakens the constraints. However, this trend changes as T_R approaches the freeze-in temperature T_{FI}. In this regime, the second moment of the momentum distribution, which also influences the Lyman-α bounds, increases with k, as shown in Eq. (2.60). This enhanced second moment strengthens the constraints and competes with the dilution effect. When $T_R \ll T_{\mathrm{FI}}$, dilution dominates and the constraints weaken with increasing k, as previously described. But as T_R approaches T_{FI}, the effect of dilution diminishes, and the growing second moment becomes the dominant factor. As a result, for fixed $T_R \lesssim T_{\mathrm{FI}}$, increasing k actually leads to stronger constraints.

In Fig. 4.2b (fermionic reheating), the constraints scale as $m_{\chi,\mathrm{FR}} \propto (T_R x_{\mathrm{FI}}/m_B)^{\frac{7-k}{3k-3}}$. As in the bosonic case, for fixed k and m_B, increasing the reheating temperature reduces dilution and results in stronger constraints. The exponent $\frac{7-k}{3k-3}$ is positive and decreases with k for $2 \leq k < 7$. Therefore, at fixed T_R and m_B, increasing k suppresses dilution and leads to stronger constraints. In this regime, the second moment also increases with k, but, as shown in Eq. (2.67), it quickly saturates to a plateau and thus contributes only marginally to the variation in constraints as k increases.

These Lyman-α constraints on FIMPs produced during bosonic and fermionic reheating demonstrate that for $2 < k < 7$, the details of the reheating history have a non-negligible impact on FIMP properties.

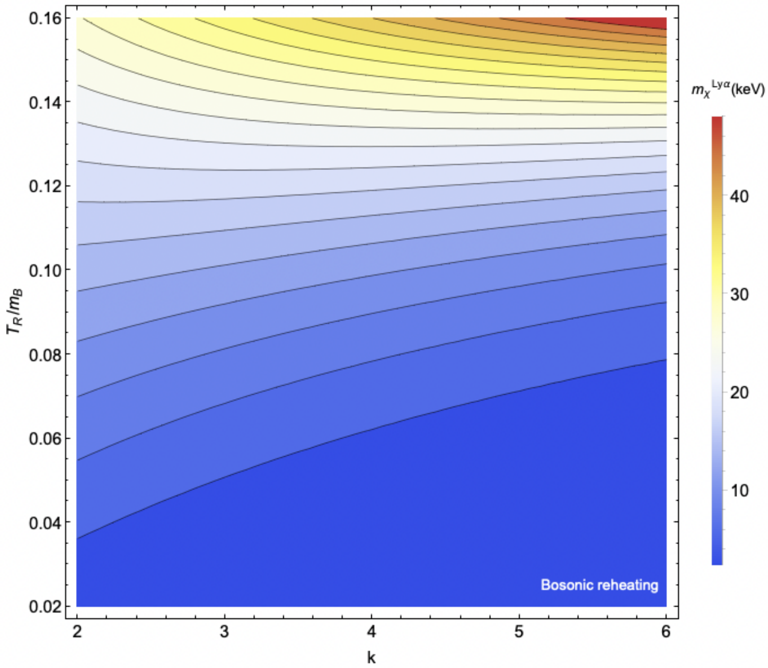

(a)

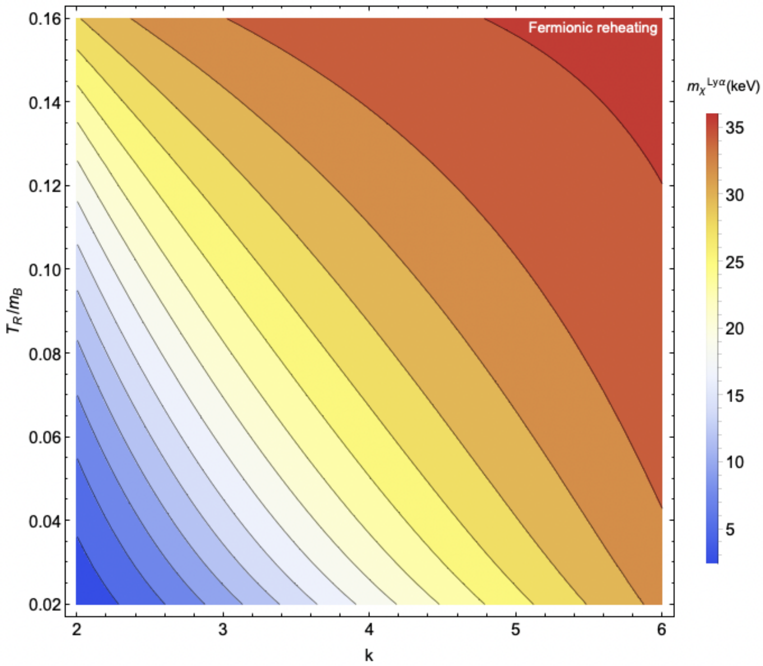

(b)

Figure 4.2: Lyman-α constraints on FIMP mass in the $(k, T_R/m_B)$ plane for **(a)** bosonic reheating and **(b)** fermionic reheating. The lower bound on the FIMP mass is indicated with a gradient of color, where red corresponds to stronger constraints and blue to weaker ones. Note that the legends differ between the two plots.

Conclusion

In this master thesis, we have investigated feebly interacting massive particles (FIMPs) as dark matter candidates, focusing on their production from freeze-in through the decay of a heavy mother particle during non-standard early cosmological scenarios. By extending the analytical framework beyond the standard radiation-dominated era, we have demonstrated that the properties of FIMPs and the resulting constraints depend significantly on the history of the early universe.

Our analysis began with the development of a general formalism to compute the momentum distribution functions of FIMPs. Starting from the Boltzmann equation, we derived analytical solutions for three distinct cosmological scenarios: the standard radiation-dominated era, an early matter-dominated era, and more general k-dominated eras where the inflaton potential follows a power-law form $V(\phi) \propto \phi^k$. For k-dominated scenarios, we further distinguished between bosonic and fermionic reheating mechanisms, which exhibit different behaviors for $2 < k < 7$.
A key result of our work is that the momentum distribution functions differ significantly between these scenarios. In the radiation-dominated era, the distribution scales as $q^{-1/2}e^{-q}$, while in an early matter-dominated era, it follows $q^{1/2}e^{-q}$. For general k-dominated scenarios, we found that the distribution scales as $q^{k-3/2}e^{-q}$ for bosonic reheating and $q^{\frac{3k-5}{2k-2}}e^{-q}$ for fermionic reheating. These differences affect the typical velocity of dark matter at production, as quantified by the second moment of the momentum distribution function.
We also computed the comoving number densities in these scenarios and identified an important effect absent in standard cosmology: entropy dilution during reheating. This dilution suppresses the final abundance of FIMPs by factors that depend strongly on both the reheating temperature and the parameter k that characterizes the inflaton potential. For bosonic reheating, this suppression scales as $(T_R/m_B)^{4k-1}$, while for fermionic reheating, it scales as $(T_R/m_B)^{\frac{9-k}{k-1}}$, highlighting the qualitatively different impacts of these reheating mechanisms. We also use the comoving number density to define the moment of freeze-in, which occurs at different times depending on the cosmological scenario considered : $x_{\rm FI} \sim 3$ in RD era, and $x_{\rm FI} \sim 6$ in non-standard cosmologies, shifting to slightly later times.
Finally, by reinterpreting existing Lyman-α constraints on warm dark matter to the case of FIMPs, we derived bounds on FIMP properties for various early cosmological scenarios, comparing their respective velocity dispersions. In the radiation-dominated era, we found a lower bound on the FIMP mass of $m_{\chi,\rm RD} \geq 16$ keV, in agreement with the literature [19]. For the early matter-dominated era, this constraint is modified by the dilution factor and the different second moment, resulting in a lower mass bound that depends explicitly on the reheating temperature and the mass of the mother particle. For k-dominated scenarios, the constraints exhibit even more complex behavior, with an opposite dependence on k for bosonic reheating and fermionic

reheating.

These results demonstrate that the early cosmological history can leave distinctive imprints on the properties of feebly interacting massive particles.

Future work could build upon and refine these results. We have shown that different cosmological scenarios lead to distinct velocity dispersions. This feature could be implemented in Boltzmann codes, such as CLASS, to study the impact of velocity dispersion on the matter power spectrum. Additionally, our constraints could be updated by incorporating the latest LHC bounds, which may significantly tighten the viable parameter space for the mother particle. Our results could also be improved by including several physical effects that were neglected in this study. For instance, thermal corrections to decay rates become important when the mother particle mass approaches the bath temperature, potentially altering the resulting momentum distributions. Moreover, the assumption of a constant number of effective relativistic degrees of freedom could be relaxed to include the temperature dependence of $g_\star(T)$, which is particularly relevant for low reheating temperatures near the era of Big Bang Nucleosynthesis.

These results can be extended further by considering alternative reheating scenarios and incorporating additional observational constraints. While this thesis has focused on a specific FIMP production mechanism via the decay of a heavy mother particle B, 2-to-2 scattering processes may also contribute significantly, especially in the regime where $m_B - m_\chi \ll m_B$. These processes could produce different momentum distributions, leading to potentially distinct Lyman-α constraints. Furthermore, the framework developed here can be applied to other dark matter candidates whose properties are shaped by early-universe dynamics, such as weakly interacting massive particles (WIMPs) [43, 46]. By comparing the resulting momentum distributions and their impact on structure formation, it may be possible to identify observational signatures that distinguish between dark matter models and shed light on the physics of the universe's earliest stages.

Bibliography

[1] H. W. Babcock, "The rotation of the andromeda nebula," *Lick Observatory Bulletin* **19** (1939) 41–51.

[2] H. I. Ewen and E. M. Purcell, "Observation of a line in the galactic radio spectrum: Radiation from galactic hydrogen at 1,420 mc./sec." *Nature* **168** no. 4283, (1951) 356–358.

[3] V. C. Rubin and W. K. Ford, Jr., "Rotation of the Andromeda Nebula from a Spectroscopic Survey of Emission Regions," *Astrophys. J.* **159** (1970) 379–403.

[4] A. Bosma, "21-cm line studies of spiral galaxies. 2. The distribution and kinematics of neutral hydrogen in spiral galaxies of various morphological types.," *Astron. J.* **86** (1981) 1825.

[5] G. Bertone and D. Hooper, "History of dark matter," *Rev. Mod. Phys.* **90** no. 4, (2018) 045002, `arXiv:1605.04909 [astro-ph.CO]`.

[6] M. Cirelli, A. Strumia, and J. Zupan, "Dark Matter," (6, 2024) , `arXiv:2406.01705 [hep-ph]`.

[7] F. Zwicky, "Die Rotverschiebung von extragalaktischen Nebeln," *Helv. Phys. Acta* **6** (1933) 110–127.

[8] H. Andernach and F. Zwicky, "English and Spanish Translation of Zwicky's (1933) The Redshift of Extragalactic Nebulae," (11, 2017) , `arXiv:1711.01693 [astro-ph.IM]`.

[9] F. Zwicky, "On the Masses of Nebulae and of Clusters of Nebulae," *Astrophys. J.* **86** (1937) 217–246.

[10] D. Clowe, M. Bradac, A. H. Gonzalez, M. Markevitch, S. W. Randall, C. Jones, and D. Zaritsky, "A direct empirical proof of the existence of dark matter," *Astrophys. J. Lett.* **648** (2006) L109–L113, `arXiv:astro-ph/0608407`.

[11] S. Junius, "Searching for feebly interacting dark matter at colliders and beam-dump experiments," *[Doctoral dissertation, ULB]* (2022) .

[12] **Planck** Collaboration, R. Adam *et al.*, "Planck 2015 results. I. Overview of products and scientific results," *Astron. Astrophys.* **594** (2016) A1, `arXiv:1502.01582 [astro-ph.CO]`.

[13] V. S. Alpher, "Ralph A. Alpher, George Antonovich Gamow, and the Prediction of the Cosmic Microwave Background Radiation," `arXiv:1411.0172 [physics.hist-ph]`.

[14] A. A. Penzias and R. W. Wilson, “A measurement of excess antenna temperature at 4080 mc/s,” *Astrophys. J.* **142** (1965) 419–421.

[15] R. H. Dicke, P. J. E. Peebles, P. G. Roll, and D. T. Wilkinson, “Cosmic black-body radiation,” *Astrophys. J.* **142** (1965) 414–419.

[16] M. Cirelli, “Dark Matter candidates, light and heavy,” *PoS* **TAUP2023** (2024) 344.

[17] M. Milgrom, “A Modification of the Newtonian dynamics as a possible alternative to the hidden mass hypothesis,” *Astrophys. J.* **270** (1983) 365–370.

[18] L. J. Hall, K. Jedamzik, J. March-Russell, and S. M. West, “Freeze-In Production of FIMP Dark Matter,” *JHEP* **03** (2010) 080, `arXiv:0911.1120 [hep-ph]`.

[19] Q. Decant, J. Heisig, D. C. Hooper, and L. Lopez-Honorez, “Lyman-α constraints on freeze-in and superWIMPs,” *JCAP* **03** (2022) 041, `arXiv:2111.09321 [astro-ph.CO]`.

[20] L. Calibbi, F. D’Eramo, S. Junius, L. Lopez-Honorez, and A. Mariotti, “Displaced new physics at colliders and the early universe before its first second,” *JHEP* **05** (2021) 234, `arXiv:2102.06221 [hep-ph]`.

[21] Q. Decant, “Non-cold dark matter imprint on cosmology,” *[Doctoral dissertation, ULB]* (2023) .

[22] L. Lopez Honorez, “GGI lecture’s note on dark matter cosmology,”.

[23] **eBOSS** Collaboration, S. Chabanier *et al.*, “The one-dimensional power spectrum from the SDSS DR14 Lyα forests,” *JCAP* **07** (2019) 017, `arXiv:1812.03554 [astro-ph.CO]`.

[24] A. A. Meiksin, “The Physics of the Intergalactic Medium,” *Rev. Mod. Phys.* **81** (2009) 1405–1469, `arXiv:0711.3358 [astro-ph]`.

[25] M. Viel, G. D. Becker, J. S. Bolton, and M. G. Haehnelt, “Warm dark matter as a solution to the small scale crisis: New constraints from high redshift Lyman-α forest data,” *Phys. Rev. D* **88** (2013) 043502, `arXiv:1306.2314 [astro-ph.CO]`.

[26] A. Garzilli, A. Magalich, T. Theuns, C. S. Frenk, C. Weniger, O. Ruchayskiy, and A. Boyarsky, “The Lyman-α forest as a diagnostic of the nature of the dark matter,” *Mon. Not. Roy. Astron. Soc.* **489** no. 3, (2019) 3456–3471, `arXiv:1809.06585 [astro-ph.CO]`.

[27] N. Palanque-Delabrouille, C. Yèche, N. Schöneberg, J. Lesgourgues, M. Walther, S. Chabanier, and E. Armengaud, “Hints, neutrino bounds and WDM constraints from SDSS DR14 Lyman-α and Planck full-survey data,” *JCAP* **04** (2020) 038, `arXiv:1911.09073 [astro-ph.CO]`.

[28] **CMS** Collaboration, A. M. Sirunyan *et al.*, “Particle-flow reconstruction and global event description with the CMS detector,” *JINST* **12** no. 10, (2017) P10003, `arXiv:1706.04965 [physics.ins-det]`.

[29] G. Bélanger *et al.*, “LHC-friendly minimal freeze-in models,” *JHEP* **02** (2019) 186, `arXiv:1811.05478 [hep-ph]`.

[30] A. Einstein, "Cosmological Considerations in the General Theory of Relativity," *Sitzungsber. Preuss. Akad. Wiss. Berlin (Math. Phys.)* **1917** (1917) 142–152.

[31] A. Friedmann, "Über die Krümmung des Raumes," *Z. Phys.* **10** (1922) 377–386.

[32] A. Friedmann, "On the curvature of space," *General Relativity and Gravitation* **31** no. 12, (1999) 1991–2000. English translation of the original 1922 paper.

[33] G. Lemaître, "Un univers homogène de masse constante et de rayon croissant rendant compte de la vitesse radiale des nébuleuses extra-galactiques," *Annales de la Société Scientifique de Bruxelles* **47** (1927) 49–59.

[34] G. Lemaître, "A homogeneous universe of constant mass and increasing radius accounting for the radial velocity of extragalactic nebulae," *Monthly Notices of the Royal Astronomical Society* **91** (1931) 483–490. English translation of Lemaître's 1927 paper.

[35] E. Hubble, "A relation between distance and radial velocity among extra-galactic nebulae," *Proceedings of the National Academy of Sciences of the United States of America* **15** no. 3, (1929) 168–173.

[36] E. W. Kolb and M. S. Turner, *The Early Universe*, vol. 69. Taylor and Francis, 5, 2019.

[37] S. Dodelson, *Modern Cosmology.* Academic Press, Amsterdam, 2003.

[38] M. Becker, E. Copello, J. Harz, J. Lang, and Y. Xu, "Confronting dark matter freeze-in during reheating with constraints from inflation," *JCAP* **01** (2024) 053, `arXiv:2306.17238 [hep-ph]`.

[39] **Planck** Collaboration, Y. Akrami *et al.*, "Planck 2018 results. X. Constraints on inflation," *Astron. Astrophys.* **641** (2020) A10, `arXiv:1807.06211 [astro-ph.CO]`.

[40] M. A. G. Garcia, K. Kaneta, Y. Mambrini, and K. A. Olive, "Reheating and Post-inflationary Production of Dark Matter," *Phys. Rev. D* **101** no. 12, (2020) 123507, `arXiv:2004.08404 [hep-ph]`.

[41] M. A. G. Garcia, K. Kaneta, Y. Mambrini, and K. A. Olive, "Inflaton Oscillations and Post-Inflationary Reheating," *JCAP* **04** (2021) 012, `arXiv:2012.10756 [hep-ph]`.

[42] R. T. Co, F. D'Eramo, L. J. Hall, and D. Pappadopulo, "Freeze-In Dark Matter with Displaced Signatures at Colliders," *JCAP* **12** (2015) 024, `arXiv:1506.07532 [hep-ph]`.

[43] N. Bernal and Y. Xu, "WIMPs during reheating," *JCAP* **12** (2022) 017, `arXiv:2209.07546 [hep-ph]`.

[44] K. J. Bae, A. Kamada, S. P. Liew, and K. Yanagi, "Light axinos from freeze-in: production processes, phase space distributions, and Ly-α forest constraints," *JCAP* **01** (2018) 054, `arXiv:1707.06418 [hep-ph]`.

[45] F. D'Eramo and A. Lenoci, "Lower mass bounds on FIMP dark matter produced via freeze-in," *JCAP* **10** (2021) 045, `arXiv:2012.01446 [hep-ph]`.

[46] N. Bernal, K. Deka, and M. Losada, "Thermal dark matter with low-temperature reheating," *JCAP* **09** (2024) 024, `arXiv:2406.17039 [hep-ph]`.